



The milk-derived lactoferrin inhibits V-ATPase activity by targeting its V1 domain

Cátia Santos-Pereira^{a,b,c}, Juliana F. Rocha^c, Henrique S. Fernandes^c, Lígia R. Rodrigues^b,
Manuela Côrte-Real^a, Sérgio F. Sousa^{c,*}

^a Centre of Molecular and Environmental Biology (CBMA), Department of Biology, University of Minho, Braga, Portugal

^b Centre of Biological Engineering (CEB), Department of Biological Engineering, University of Minho, Braga, Portugal

^c UCIBIO@REQUIMTE, BioSIM, Departamento de Biomedicina, Faculdade de Medicina da Universidade do Porto, Porto, Portugal

ARTICLE INFO

Keywords:

Lactoferrin
V-ATPase
Docking
Molecular dynamics

ABSTRACT

Lactoferrin (Lf), a bioactive milk protein, exhibits strong anticancer and antifungal activities. The search for Lf targets and mechanisms of action is of utmost importance to enhance its effective applications. A common feature among Lf-treated cancer and fungal cells is the inhibition of a proton pump called V-ATPase. Lf-driven V-ATPase inhibition leads to cytosolic acidification, ultimately causing cell death of cancer and fungal cells. Given that a detailed elucidation of how Lf and V-ATPase interact is still missing, herein we aimed to fill this gap by employing a five-stage computational approach. Molecular dynamics simulations of both proteins were performed to obtain a robust sampling of their conformational landscape, followed by clustering, which allowed retrieving representative structures, to then perform protein-protein docking. Subsequently, molecular dynamics simulations of the docked complexes and free binding energy calculations were carried out to evaluate the dynamic binding process and build a final ranking based on the binding affinities. Detailed atomist analysis of the top ranked complexes clearly indicates that Lf binds to the V₁ cytosolic domain of V-ATPase. Particularly, our data suggest that Lf binds to the interfaces between A/B subunits, where the ATP hydrolysis occurs, thus inhibiting this process. The free energy decomposition analysis further identified key binding residues that will certainly aid in the rational design of follow-up experimental studies, hence bridging computational and experimental biochemistry.

1. Introduction

Lactoferrin (Lf) is a single-chain iron-binding protein with a molecular weight of about 80 kDa that belongs to the transferrin family. It was identified in several biological body fluids of mammalian species including numerous mucosal surfaces and also in the specific granules of neutrophils. However, its main sources are by far milk and colostrum, reason why it is often called a milk-derived protein [1]. The tertiary structure of the human Lf (hLf) was determined more than 30 years ago and revealed that it is folded into two symmetric globular lobes (N and C for N- and C-terminal lobes, respectively) that are connected by an alpha-helix. Each lobe is further divided in two sub-domains (N1 and N2; C1 and C2) [2]. Lf exhibits an overall high homology among species. Indeed, the structure of bovine Lf is very similar to that of hLf [3] and both proteins share 69% of sequence similarity [4]. Lf can exist in the

iron-free form (apo-Lf) or saturated with iron (holo-Lf). It has two very similar iron-binding sites (one in each lobe), thus, in its holo-form, two Fe³⁺ ions are bound in association with two carbonate anions. One of the most distinct features of Lf is its highly cationic character that has been demonstrated to be crucial for its interaction with a variety of molecules [5].

A myriad of biological activities have been attributed to Lf throughout the years including immunomodulatory, antimicrobial, anti-inflammatory, anticancer, among other functions, which are the basis of its well-recognized multifunctionality [6]. In the search for the molecular mechanisms underlying both the Lf anticancer and antifungal activities, in our previous work, we identified for the first time the proton pump V-ATPase as a Lf target [7–9]. V-ATPases are multi-subunit proton pumping ATPases well conserved from prokaryotes to eukaryotes, which are present in a diverse collection of biological membranes, coupling the

* Corresponding author at: UCIBIO@REQUIMTE, BioSIM, Departamento de Biomedicina, Faculdade de Medicina da Universidade do Porto, Alameda Professor Hernani Monteiro, 4200-319 Porto, Portugal.

E-mail address: sergiosousa@med.up.pt (S.F. Sousa).

<https://doi.org/10.1016/j.ijbiomac.2021.06.200>

Received 7 April 2021; Received in revised form 20 June 2021; Accepted 29 June 2021

Available online 5 July 2021

0141-8130/© 2021 Elsevier B.V. All rights reserved.

energy of ATP hydrolysis to actively pump protons. They are divided in two functional domains, the cytosolic V_1 domain, where the ATP hydrolysis takes place; and the membrane-embedded V_o domain, where protons are translocated. Each domain comprises different subunits with defined stoichiometry that together form a complex of about 1 MDa with 30 subunits [10]. In yeast, the V_1 domain contains the subunits A_3 , B_3 , C , D , E_3 , F , G_3 , and H [11]; while the V_o domain is composed by subunits a , d , e , f , the assembly factor $Voa1$, as well as a c -ring that consists of subunits c_8 , c' and c'' [12]. Subscript numbers indicate the subunit

stoichiometry. V-ATPases operate through a rotary mechanism in which the chemical energy resulting from ATP hydrolysis at the AB subunits is converted into mechanical energy to promote the rotation of a central rotor (composed by subunits D and F from the V_1 domain as well as d and the c -ring from the V_o domain) [13]. This rotation, in relation to the C-terminal membrane embedded part of the a subunit, prompts the proton transport across the membranes by highly conserved glutamate residues in the c -ring. These residues become protonated in a half channel accessible from the cytosolic side and release the proton in the half

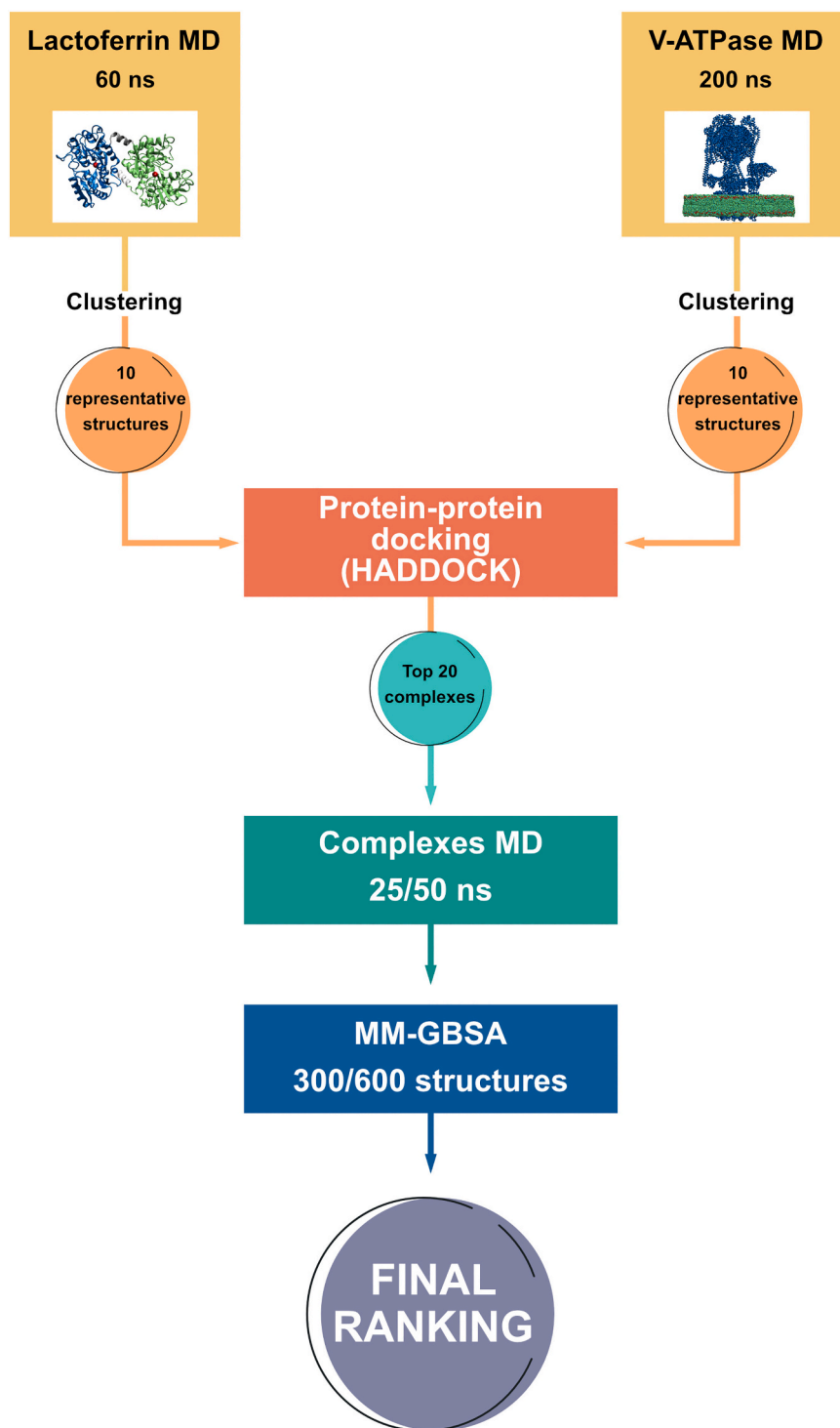


Fig. 1. Flowchart of the computational pipeline used in this work. ns, nanoseconds; MD, molecular dynamics; HADDOCK, High Ambiguity Driven protein–protein Docking; MM-GBSA, Molecular Mechanics/Generalized Born Surface Area.

channel accessible from the other side of the membrane after rotation [14]. Mutations or defects in V-ATPase have been associated with a plethora of human diseases [15].

Regarding Lf anticancer activity, we found that this protein is selectively cytotoxic to highly metastatic cancer cells displaying V-ATPase at the plasma membrane. In contrast, lowly metastatic cancer cells or non-cancer cells that exhibit only intracellular V-ATPase are resistant to Lf. This selectivity was associated not only with the presence of V-ATPase at the plasma membrane of highly metastatic cancer cells, but also to its higher activity and expression in this type of cells. Accordingly, the basal extracellular acidification rate, which is mainly maintained by plasmalemmal V-ATPase, greatly decreased after Lf treatment, leading to a concomitant intracellular proton accumulation and cytosolic acidification. Furthermore, Lf also hindered lysosomal acidification of highly metastatic cancer cells, suggesting that both plasma membrane and lysosomal V-ATPases are inhibited by Lf, possibly boosting the observed cytosolic acidification after Lf treatment. This cascade of events culminates in apoptosis induction and cell death [7,8]. In addition, by isolating lysosomes from rat liver, which are enriched in V-ATPase, we showed that Lf inhibits both the V-ATPase proton pumping and hydrolytic activities [7].

More recently, we were focused on unraveling the molecular basis of the antifungal activity of Lf, using the yeast *Saccharomyces cerevisiae* as a model. We found that Lf induces vacuolar alkalization, which is largely ensured by V-ATPase, in whole cells as detected by the increase in the fluorescence of a pH-sensitive probe. Moreover, by isolating yeast purified vacuoles, we showed that the proton pumping activity of the yeast V-ATPase was inhibited by Lf in a concentration-dependent manner [9]. This Lf effect, together with its inhibitory action towards the plasma membrane proton pump Pma1p and disruption of ergosterol-rich lipid rafts [9], lead to an apoptosis-like cell death in yeast [16].

Though our previous studies identified V-ATPase as a Lf target in both yeast and highly metastatic human cancer cells, the molecular basis of this interaction is still unknown. Therefore, in this work, we sought to develop a computational approach to understand how Lf and V-ATPase interact and to shed light on the putative residues of both proteins that are critical for the interaction. For this purpose, an *in silico* approach that takes into account different conformational states of both proteins was used to predict the protein-protein complexes by molecular docking, followed by further refinement through molecular dynamics simulations and free energy calculations.

2. Methods

2.1. Overview

The computational pipeline used in this work is depicted in Fig. 1. Before performing molecular docking, which is a computational method used to predict the preferred binding pose(s) between two molecules [17], molecular dynamics (MD) simulations of V-ATPase and Lf were carried out. MD is a technique that integrates the Newton's equation of motion for predicting the movements of atoms given the position of the surrounding atoms, as a function of time [18]. This generated a series of conformations of both proteins in solution that were then clustered to identify 10 representative structures of each protein, which were later used in the molecular docking study. This approach allows the sampling of several protein conformations and, consequently, of their interaction. Afterwards, the molecular docking software HADDOCK (High Ambiguity Driven protein-protein Docking) [19] was used to predict the complexes between V-ATPase and Lf. The best scored 20 complexes generated by HADDOCK were then embedded into a membrane bilayer model and subjected to MD simulations. The Molecular Mechanics/Generalized Born Surface Area (MM/GBSA) method [20] was next applied to the equilibrated part of these MD simulations to rescore the complexes based on the free binding energy. Moreover, it was used to calculate the individual contribution of each amino acid and predict the

residues from both proteins that are more important for the protein-protein association.

2.2. Lactoferrin model setup and molecular dynamics simulations

After a literature review and search on the Protein Databank (<https://www.rcsb.org>) of all available Lf structures, the 1LFG structure of diferric human lactoferrin [21], obtained by X-ray crystallography at a resolution of 2.2 Å without any mutation, was chosen. The PropKA server version 3.0 [22] was employed to predict the protonation states of the different amino acid residues considering the physiological pH (pH 7). Lysine and arginine residues were modelled as positively charged, while aspartate and glutamate residues as negatively charged. Histidine residues were modelled as neutral, with a hydrogen at the epsilon-N or delta-N according to the surrounding.

The 1LFG structure contains two iron-binding sites, where one Fe³⁺ and one CO₃²⁻ ions are present along with two tyrosine, one aspartate and one histidine residues. The iron-coordinated tyrosine and histidine residues (Tyr92, Tyr192, His253, Tyr435, Tyr528 and His597) were modelled as deprotonated according to the literature [23]. The iron coordination spheres were parameterized using the python-based metal center parameter builder MCPB.py with the bonded model approach [24]. These calculations were performed by quantum mechanics using the Gaussian 09 [25] software with Density Functional Theory (DFT) and the B3LYP [26,27] functional and 6-31G(d) [28–32] basis set [33]. MCPB and the bond-model approach have been well validated in the past for the simulation of several different metalloproteins and enzymes [34,35]. The system was prepared using AMBER 19 software package [36]. The LEAP program was used to add the hydrogen atoms and to build the topology and parameters of the protein with the biomolecular force fields *ff14SB* [37] for proteins, and the general amber force field *gaff2* [38] for organic molecules. Periodic boundary conditions were applied in all directions using a cubic box with a minimum distance between the protein and the box wall set to 12 Å. Water molecules were added to the system using the TIP3P function and the *tip3p* force field for water and associated ions. K⁺ and Cl⁻ ions were randomly added to the system to neutralize charges, as well as to achieve a 0.15 M concentration, which approaches the physiological regime. The dimension of the system was 92,889 atoms. The system was then submitted to a 4-step energy minimization process using the SANDER module from AMBER 19 to remove clashes before the MD simulation. Firstly, harmonic forces were used to restrain all atoms positions except those from water molecules (5000 steps), then constraints were applied only to the heavy atoms allowing the energy minimization of the hydrogen atoms (5000 steps), next only to the backbone alpha carbons (C α) and nitrogens were constrained (5000 steps), and finally all constraints were removed to allow a full energy minimization (25,000 steps). A 20 ps equilibration was subsequently performed in the canonical thermodynamic (NVT) ensemble with constant volume, where the temperature of the system was gradually increased to 303.15 K (30 °C) using Langevin thermostat [39,40]. A 60 ns simulation was then conducted with Gromacs software [41] in an isothermal-isobaric thermodynamic ensemble (NPT) at 303.15 K using the Berendsen temperature coupling scheme [42]. Pressure was maintained constant (1 bar) using the Parrinello-Rahman barostat [43] with isotropic molecule-based scaling. Particle-Mesh Ewald (PME) method was used for long-range electrostatics, and the non-bond interaction cut-off radius was set to 10 Å. The bond lengths involving hydrogen atoms were constrained using the linear constraint solver (LINCS) algorithm [44], allowing the integration of the equation of motion with a 2 fs time step. The MD trajectory was sampled every 2 ps. The MD simulation was analysed in terms of backbone root-mean-square deviation (C α -RMSD), backbone root-mean-square fluctuation (RMSF), solvent accessible surface area (SASA), and principal component analysis (PCA) for all heavy atoms of the protein using the CPPTRAJ module of AMBER 19. Clustering was performed with values retrieved from the last 55 ns of the simulation using the hierarchical

agglomerative approach, which is based on the distance between frames calculated via the C α -RMSD, to obtain 10 representative structures of the MD trajectory for further docking analysis.

2.3. Modeling of V-ATPase and molecular dynamics simulations

At the time this work started, no human V-ATPase structure was available, thus a list of all V-ATPase structures from *Saccharomyces cerevisiae* was compiled. From all those structures, only three contained the biological assembly of the entire complex (3J9T-V, 6O7V-X and 5VOX-Z) obtained by cryo-electron microscopy (cryo-EM) with poor resolution values (6.6–6.9 Å). Structure 6OTV [45], which has the better resolution, has only backbone information and no sidechains. Thus, we chose the 3J9T [11], which has backbone and sidechains of all residues. However, this structure misses some subunits of the V_o domain namely, subunits *e* and the assembly factor Voa1, and does not distinguishes between *c*, *c'* and *c''* subunits. In this sense, through molecular modeling, we constructed a structure that contains the V₁ subunits of 3J9T and the V_o subunits of 6O7T [45]. The latter has a much better resolution (3.2 Å) and all the subunits. Very recently, the first cryo-EM structure of human V-ATPase at up to 2.9 Å resolution was reported revealing an overall similar structure with our model [46]. After building the system, the PACKMOL-memgen tool [47] from Ambergtools was used to build a membrane lipid bilayer system, where V-ATPase was embedded and positioned parallel to the vertical axis of the membrane. The choice of the lipid types and ratios was based on a work performed by Jo and co-workers [48], who built lipid bilayers that resemble yeast membranes. Thus, the membrane is composed of dipalmitoyl phosphatidylcholine (DPPC), dioleoyl phosphatidylcholine (DOPC), 1-palmitoyl-2-oleoyl phosphatidylethanolamine (POPE), 1-palmitoyl-2-oleoyl phosphatidylamine (POPA), 1-palmitoyl-2-oleoyl phosphatidylserine (POPS) and cholesterol (CHL) in a ratio of 2:10:6:2:1, respectively. The system was placed in a rectangular TIP3P water box with a minimum distance between the protein and the box boundaries of 15 Å, and periodic boundary conditions. Protonation states for all amino acids at pH 7 were considered. The width of the leaflet was set to 23 Å. K⁺ and Cl⁻ ions were included to neutralize the charges and to achieve a final concentration of 0.15 M, as above described for Lf. The size of the system was 1,802,167 atoms. In addition to the force fields used for Lf MD, the *lipid17* force field [49] was also used for the V-ATPase MD simulation. The system was then subjected to a five-stage refinement protocol using the SANDER module from AMBER 19, in which constrains in the protein/lipids were progressively removed. In the first stage, constraints were applied to all atoms except water (5000 steps); in a second stage, the constraints were limited to all heavy atoms allowing the hydrogens added by the LEAP program from AMBER 19 to adjust (5000 steps); in a third stage, constraints were removed from the lipid atoms to allow their fine-tuning (5000 steps); in a fourth stage, only the backbone atoms were constrained (5000 steps); and finally, in the fifth stage, all constraints were removed and a full energy minimization of the system (50,000 steps) was performed. Next, the system was heated to 303.15 K by two sequential equilibration runs keeping the lipids fixed by applying a harmonic restraint of 10 kcal/(mol Å²). The MD simulations were carried out using the PMEMD module of AMBER 20 [50]. First the system was heated to 100 K using a Langevin thermostat in a NVT ensemble (50 ps); and, in the second step, heated to the production temperature of 303.15 K using a semi-isotropic Berendsen barostat to equilibrate the pressure in a NPT ensemble (50 ps). Aiming to equilibrate the system's periodic boundary dimensions and density, a hold step of 125 ps was performed before MD production, where the lipid restraints were removed and the width of the non-bonded "skin" was increased to 5 Å to cope with the changes in box dimensions during simulation. All production MD simulations were done in the NPT ensemble using the Langevin thermostat to maintain temperature at 303.15 K. Surface tension was kept constant in the xy plane using the semi-isotropic Berendsen pressure coupling algorithm with the pressure

set to 1 bar. The time step was 2 fs and the non-bonded interaction cut-off radius was set to 10 Å. Bond lengths using hydrogens were constrained using the SHAKE algorithm [51]. A total simulation time of 200 ns was reached. The trajectory was sampled every 10 ps. Analysis of the MD simulation in terms of SASA, C α -RMSD, RMSF, and PCA for all heavy atoms of the protein was carried out with the CPPTRAJ module of AMBER 19. Clustering was performed with values retrieved from the last 125 ns of the simulation using the hierarchical agglomerative approach to obtain 10 representative structures of the MD trajectory to be used in the docking step. Visual Molecular Dynamics (VMD) [52] was used for all visualizations.

2.4. Protein-protein docking using HADDOCK

The HADDOCK 2.4 webserver [53] was used to predict the complexes between V-ATPase and Lf. Each of the 10 representative structures of the Lf MD trajectory were docked with the 10 representative structures derived from the V-ATPase MD. Due to the large number of V-ATPase atoms, the protein was separated into the two domains (V_o and V₁) and submitted for docking with Lf, which resulted in a total of 200 independent docking runs. Also, due to the large V-ATPase size, when defining HADDOCK settings, the coarse grain option with Martini [54] was activated. Since there is no data on the possible binding site, no active or passive residues were defined. Instead, random patches, where ambiguous interaction restraints (AIRs) are randomly defined from accessible residues (>20% relative accessibility), were used. Since we did not define semi-flexible segments, all accessible residues were considered. For each docking trial, a different residue from both proteins, as well as their neighbors within 5 Å were selected. For this reason, the sampling was increased to 10,000/400/400 structures for it0, it1 and itw stages, respectively. Clustering was performed using the fraction of common contacts (FCC) with a cut-off of 0.6 and a minimum cluster size of 4. The FCC clustering metric calculates the fraction of inter-protein residue pairs which are common between complexes [55]. The HADDOCK score (HS) was used to narrow down the large number of possibilities of protein-protein interactions to a small subset. The HS function is a linear weighted sum of energetic terms and buried surface area ($HS = 1E_{vdw} + 0.2E_{elec} + 1E_{desol} + 0.1E_{AIR}$), where each term corresponds to van der Waals, Coulomb electrostatics, desolvation and restraint energies, respectively [56]. The OPLS force field [57] is used to calculate the non-bonded terms (E_{vdw} and E_{elec}), while the E_{desol} is calculated via a SASA-dependent empirical term that estimates the energetic gain/penalty of burying specific parts of the protein when the complex is formed [56]. The top 10 structures from each run were first selected and, afterwards, only the solutions with HS below -150 and whose Lf binding site was not located in the V-ATPase regions that are embedded in the cellular membranes were considered. From those, the top 20 were selected to proceed to MD simulations.

2.5. Molecular dynamics simulations of V-ATPase-Lf complexes

After being embedded into a lipid bilayer using PACKMOL-memgen as aforementioned, the 20 top docked complexes were further refined from their docking poses by 25 ns MD simulations using the same MD protocol above described for V-ATPase. For the top 4 complexes, the MD simulations were further extended to 50 ns. RMSD and SASA analysis were performed as above stated with CPPTRAJ.

2.6. Binding free energies calculations by the MM-GBSA method

The MM-GBSA method was employed to calculate the binding Gibbs free energy (ΔG_{bind}) of each docking solution and to rank them according to their binding affinities. This method exhibits a good balance between computational cost and accuracy [58], is widely used to predict protein-protein binding affinities and to evaluate docking solutions [59]. Moreover, it allows the identification of the dominant interactions

in a given complex by performing free energy decomposition analysis, which calculates the detailed energetic contributions of the individual residues to the system binding [58]. The MM-PBSA.py script [60] from AMBER 20 [50] was herein used to calculate the binding free energies of each complex and the energy decomposition method was applied to all residues. A total of 300 structures retrieved from the last 10 ns of each complex MD simulation were used for the analysis of the top 20 complexes. For the 50 ns simulations of top 4 docked complexes, additional MM-GBSA calculations were performed with 600 snapshots retrieved from the equilibrated region (15–50 ns). The ΔG_{bind} for each complex, as well as for the residues displaying a higher contribution for the top 4 complexes, are presented.

The free energy of binding is calculated from the difference between the total free energy variation when molecules are in bounded or non-bounded state (Eq. (1)).

$$\Delta G_{bind} = \Delta G_{complex} - (\Delta G_{protein1} + \Delta G_{protein2}) \quad (1)$$

If $\Delta G_{complex}$ is lower (i.e. more negative) than the sum of the ΔG of the separated proteins, then the ΔG_{bind} is negative and the association of the proteins is thermodynamically favorable. In the MM-GBSA method, the ΔG_{bind} can be described by the sum of different energy terms (Eq. (2)):

$$\Delta G = \Delta E_{gas} + \Delta G_{sol} - T\Delta S \quad (2)$$

$$\Delta E_{gas} = \Delta E_{int} + \Delta E_{ELE} + \Delta E_{VDW} \quad (3)$$

$$\Delta G_{sol} = \Delta G_{GB} + \Delta G_{Surf} \quad (4)$$

These energy contributions were computed from the atomic coordinates of the V-ATPase, Lf and the complex. The gas-phase interaction energy (ΔE_{gas}) between V-ATPase and Lf is the sum of electrostatic (ΔE_{ELE}) and van der Waals (ΔE_{VDW}) interaction energies. Since V-ATPase, Lf and the complex V-ATPase-Lf were extracted from the same trajectory, the internal energy change (ΔE_{int}) cancels out (Eq. (3)). Both polar and non-polar solvation free energy terms contribute to the solvation free energy (ΔG_{sol}) (Eq. (4)). The polar solvation free energy (ΔG_{GB}) is calculated through a modified Generalized Born (GB) method [20]. The non-polar contribution to the solvation free energy (ΔG_{Surf}) is based on the calculation of the SASA by the Linear Combinations of Pairwise Overlaps (LCPO) method [61]. The entropy term (T ΔS) was neglected in the calculation as it is computationally expensive for large systems and tends to introduce low accurate approximations [60].

3. Results and discussion

Lf was shown to inhibit V-ATPase activity in three different models: yeast [9], highly metastatic cancer cells and liver lysosomes [7]. However, the molecular basis of this interaction has not been disclosed being the focus of this work. X-ray crystallography or cryo-EM provides static pictures of the macromolecules that do not always represent the main conformation of the proteins in solution [62]. Moreover, before complexation with a binding partner, proteins undergo changes to conformational states that are more predisposed to form a stable complex [63]. In this context, one of the main bottlenecks of the docking programs is to not take into account the full extent of conformational changes exhibited by the unbound proteins. To mitigate these pitfalls, first, MD simulations of Lf and V-ATPase in water and clustering analysis were conducted to obtain a robust sampling of the conformational landscape of both proteins. Approaches with the same goal have been previously shown to improve the reliability of the generated docking poses [63].

3.1. General analysis of the Lf MD simulation

Prior to the docking study, an overall analysis of the MD trajectories that generated different protein conformations to be used in the docking study was performed. Lf structural behaviour along the trajectory was

evaluated using the root-mean-square deviation (RMSD) of the protein C α . It raises in the first 2.5 ns and then reaches a plateau that exhibits maximal values of deviation of 3–4 Å (Fig. 2A), indicating that the simulation is stabilized and that the overall structure of the protein was well maintained. For this reason, the last 55 ns of the simulation were considered for all the subsequent analysis. The simulation time computed in this work is in accordance with previous reports [23,64–66]. The behaviour of the individual amino acid residues was also evaluated through root-mean-square fluctuation (RMSF) analysis, where maximal values of 3 Å were obtained, supporting that the Lf structure does not suffer significant fluctuations throughout the MD simulation (Fig. 2B). We also assessed the total solvent accessible surface area (SASA) as a measure of the area of the protein prompt to interact with other molecules. It is well stabilized since the beginning of the simulation with an average of $27,202 \pm 376 \text{ \AA}^2$ (Fig. 2C). The PCA for the Lf MD simulation showed a first mode associated with a convergent tilt of the two main protein domains (Fig. S1A). This movement accounts for 65.45% of all the computed modes. The second most prevalent mode accounts for 13.98% and it is widely sampled across the main mode (Fig. S1B).

Afterwards, a clustering method based on the best-fit coordinate RMSD was used taking into account the likeness and conformational variability among the structures generated during the MD simulation, important aspects for the subsequent stages. 10 clusters were created and the total number of frames in each cluster as well as the distribution of the cluster populations along the simulation is depicted in Fig. S2. A representative/average structure from each cluster was selected and used in the docking stage.

3.2. General analysis of the V-ATPase MD simulation

The V-ATPase model assembled in this study can be observed in Fig. 3A, where all its 16 subunits are identified. The system was then embedded into a lipid bilayer and subjected to a long MD simulation of 200 ns, which is in accordance with previous publications on membrane transporters [67–69]. Since this system is much larger than that of Lf (1,802,167 vs 92,889 atoms), a higher simulation time was required to reach equilibrium. The C α -RMSD undergoes a sudden augment in the first ns of the simulation, then increasing slightly until 125 ns, moment from which the trajectory stabilizes, and the model is well equilibrated exhibiting an average deviation from the initial structure of 7 Å for the entire complex and of 6.5 Å for the V₁ domain. In contrast, the C α -RMSD of the V_o domain atoms stabilizes right in the beginning of the MD simulation, showing a much lower average deviation value – 4.0 Å (Fig. 3B; Table 1, 2nd column). Taking into account these observations, the last 125 ns were considered for the clustering analysis. Regarding the SASA of the entire complex, it increases in the first nanoseconds of the simulation and then stabilizes to an average of $318,731 \pm 1394 \text{ \AA}^2$, with no significant changes being observed along the simulation (Fig. 3C). From these, an average of about $92,000 \text{ \AA}^2$ is devoted to the V_o domain, while about $226,000 \text{ \AA}^2$ are accessible to the solvent in the V₁ domain (Table 1, 4th column). From these data, it is clear that the majority of the V-ATPase area available to interact with other molecules is located at the cytosolic domain. As for the PCA for this simulation, the first PCA mode is associated with an anticlockwise rotation of the cytosolic domain (Fig. S3C). The second most important PCA mode has a comparable percentage of preponderancy and corresponds to a slight adjustment of the V-ATPase membrane domain. The normalized histogram of PCA1 vs PCA2 shows that both movements are not independent (Fig. S3). On the other hand, the PCA3 seems to be widely sampled across the PCA1 mode (Fig. S3B), suggesting uncoupled global drifts.

The analysis of the behaviour of the individual subunits along the MD simulation revealed that E and G subunits are those that undergo a higher deviation from the initial structure reaching an average C α -RMSD of 8.2 Å and 8.7 Å, respectively, in the last 75 ns of the simulation. Subunits A, C, a and c'' display an average C α -RMSD of about 4 Å, while

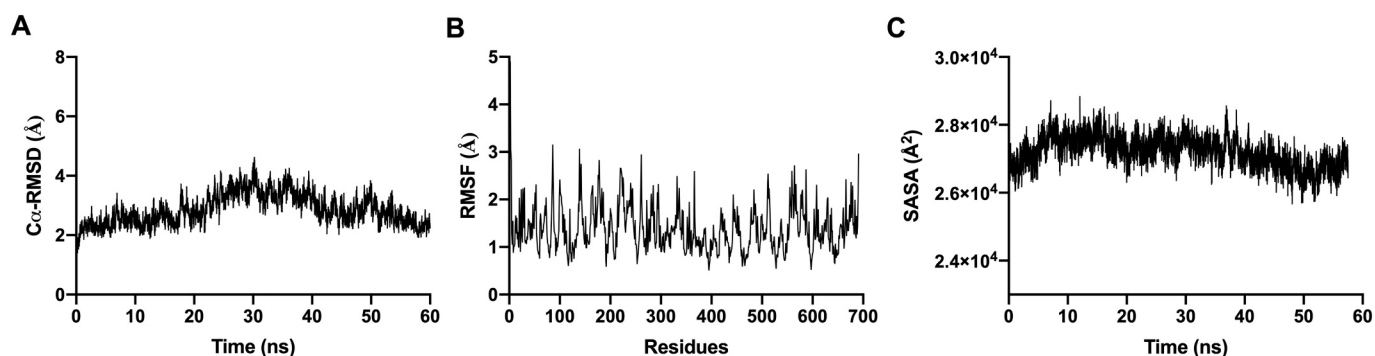


Fig. 2. Lactoferrin molecular dynamics simulation analysis. (A) RMSD values of the protein backbone C α atoms as a function of time for the 60 ns of the Lf MD simulation, with the final minimized and equilibrated structure as a reference point. (B) RMSF values of the backbone atoms as a function of time for the equilibrated region of the Lf MD simulation (last 55 ns). (C) Variation of the Lf solvent accessible surface area (SASA) along the 60 ns of the simulation.

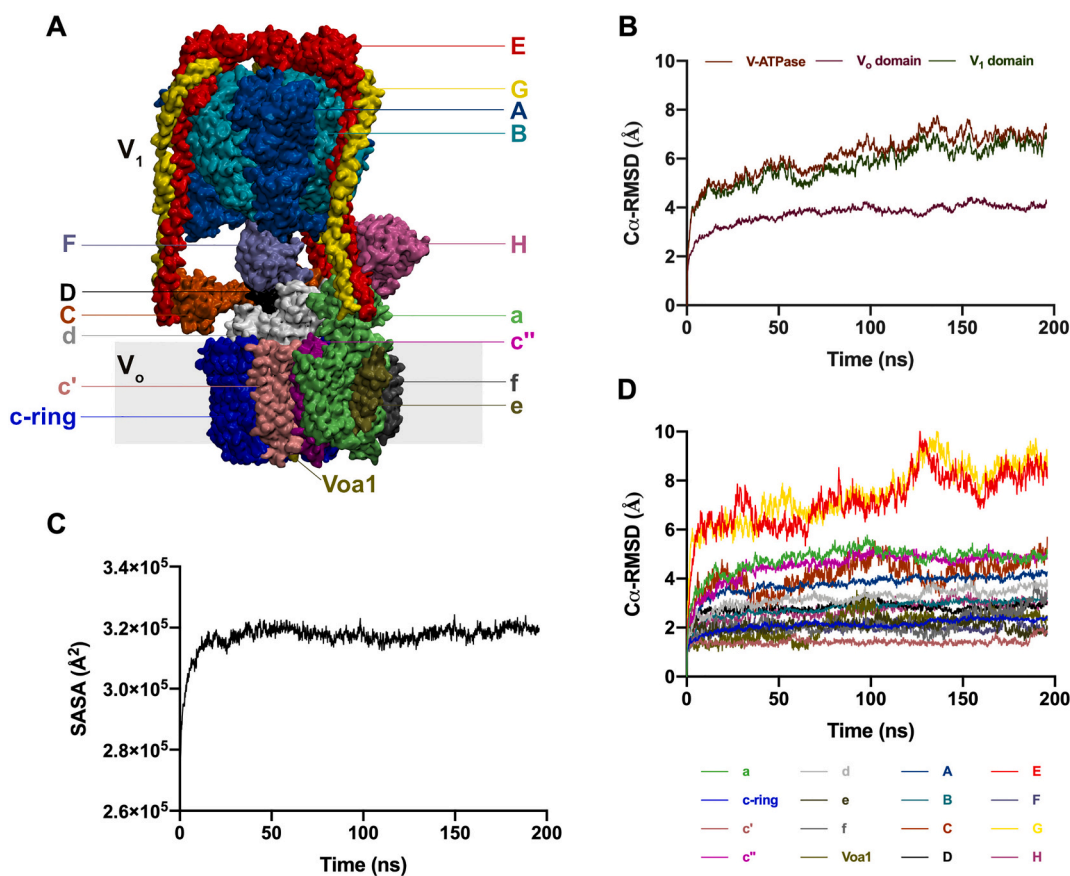


Fig. 3. V-ATPase molecular dynamics simulation analysis. (A) Structure of the V-ATPase model assembled in this work with each subunit identified in a different colour. (B) RMSD representation of the protein C α atoms as a function of time for the 200 ns of the simulation. The RMSD of atoms belonging to the membrane (V₀) or cytosolic (V₁) domains is also depicted. (C) Variation of the V-ATPase solvent accessible surface area (SASA) along the 200 ns of simulation. (D) C α -RMSD of the atoms belonging to the individual V-ATPase subunits. RMSD values for subunits A, B, E and G correspond to atoms belonging to 3 different chains each whereas the c-ring contains atoms of 8 different chains. (For interpretation of the references to colour in this figure legend, the reader is referred to the web version of this article.)

the values for the other subunits are below 3.5 Å (Fig. 3D; Table 1, 2nd column). Although these values are slightly high, they are acceptable for regions that are very exposed to the solvent as it is the case of subunits A, a, C, E and G, as it can be observed in Fig. 3A. Moreover, these values are within the expected range for a protein that was modulated and whose resolution is not the ideal. Contrary to this, no important variations were observed when the average root mean square fluctuations (RMSF) for all the residues of each subunit, which ranged from 2.0 to 4.1 Å, was analysed (Table 1, 3rd column). The SASA values were in accordance with the size of each subunit and remained almost constant along the last 75

ns of the simulation as indicated by the low standard deviation values (Table 1, 4th column).

From the last ns of the V-ATPase simulation, 10 clusters were generated and a representative structure from each cluster was used in the docking protocol. Fig. S4 shows the total number of frames in each cluster and the distribution of the cluster populations during the simulation time.

Table 1

Analysis of the last 75 ns of the V-ATPase molecular dynamics simulation. Average values of the backbone RMSD, RMSF and SASA calculated from the last 75 ns of the V-ATPase simulation for the whole system, the two domains and the individual subunits. Values are Å or Å² ± standard deviation.

V-ATPase/domain/subunit	C α -RMSD (Å)	RMSF (Å)	SASA (Å ²)
V-ATPase	7.0 ± 0.2	2.6 ± 0.6	318,731 ± 1394
V _o domain	4.0 ± 0.1	2.4 ± 0.4	92,727 ± 884
V ₁ domain	6.5 ± 0.2	2.7 ± 0.7	226,005 ± 1105
A	4.1 ± 0.1	2.4 ± 0.5	67,603 ± 570
B	3.1 ± 0.1	2.2 ± 0.4	45,713 ± 529
C	4.4 ± 0.3	3.2 ± 0.6	20,027 ± 331
D	2.8 ± 0.1	4.1 ± 1.7	9617 ± 226
E	8.2 ± 0.4	3.9 ± 1.0	36,157 ± 387
F	2.0 ± 0.2	2.0 ± 0.3	5037 ± 235
G	8.7 ± 0.4	3.6 ± 0.8	19,630 ± 233
H	3.0 ± 0.1	3.0 ± 0.6	21,993 ± 328
a	4.9 ± 0.1	2.3 ± 0.3	29,098 ± 515
c-ring	2.3 ± 0.1	2.5 ± 0.4	32,892 ± 601
c'	1.4 ± 0.1	2.7 ± 0.3	4351 ± 172
c''	4.8 ± 0.1	2.5 ± 0.4	5971 ± 177
d	3.5 ± 0.1	2.1 ± 0.3	14,068 ± 256
e	2.1 ± 0.2	2.5 ± 0.3	1773 ± 129
f	2.4 ± 0.4	2.7 ± 0.5	1860 ± 180
Voa1	2.4 ± 0.1	2.7 ± 0.5	2503 ± 87

3.3. V-ATPase-Lf molecular docking

After clustering, the sampled structures from the Lf and V-ATPase MD simulations were subjected to protein-protein molecular docking with the HADDOCK 2.4 software using the ab-initio mode, which defines random restrains considering all the solvent accessible residues with relative accessibility higher than 20%. From these calculations,

numerous complexes that predict the preferable binding pose between Lf and V-ATPase were generated. Only the solutions obtained after the final refinement in water were considered. The Haddock scoring function considers several aspects of biomolecular recognition by combining van der Waals, Coulomb electrostatics, desolvation and restraint energies, and was used in this work to rank the complexes since it was previously shown to have high success rates [56]. Considering the Haddock score and the visual analysis to discard those complexes in which Lf was docked in the V-ATPase membrane region, the top 20 complexes were selected (Fig. 4, Table 2). Consistently, all the best scored complexes exhibited Lf docked in the cytosolic V₁ domain with a good exploration of the conformational space (Fig. 4, Movie S1). All the selected complexes showed a good (negative) Haddock score ranging from −202.8 to −151.4 and a buried surface area that ranged from 3535 to 1733 Å² (Table 2, 2nd and 5th columns). Van der Waals and electrostatic interactions seem to favor the binding in all cases (Table 2, 3rd and 4th columns).

Taking a closer look to the Lf-binding subunit in each complex (Table 2, 6th column), in 85% of the top 20 complexes Lf binds to the A subunits, in 60% to E subunits, in 40% to B subunits, in 35% to G subunits and in 15% to the H subunit. Clearly, there is a Lf preference to bind to the V-ATPase region responsible for ATP hydrolysis. Each V-ATPase has three subunits A and B that together form the so-called catalytic hexamer A₃B₃. They are located in an alternating fashion comprising three ATP-hydrolyzing catalytic sites in the AB interfaces. During rotational catalysis, the AB pairs undergo conformational changes to accomplish the ATP hydrolysis [11,45,46], adopting an “open”, “loose” or “tight” conformation depending on whether they are nucleotide-free, bound to ADP or to ATP, respectively [11]. Work performed with the *Enterococcus hirae* V-ATPase shed some light on the

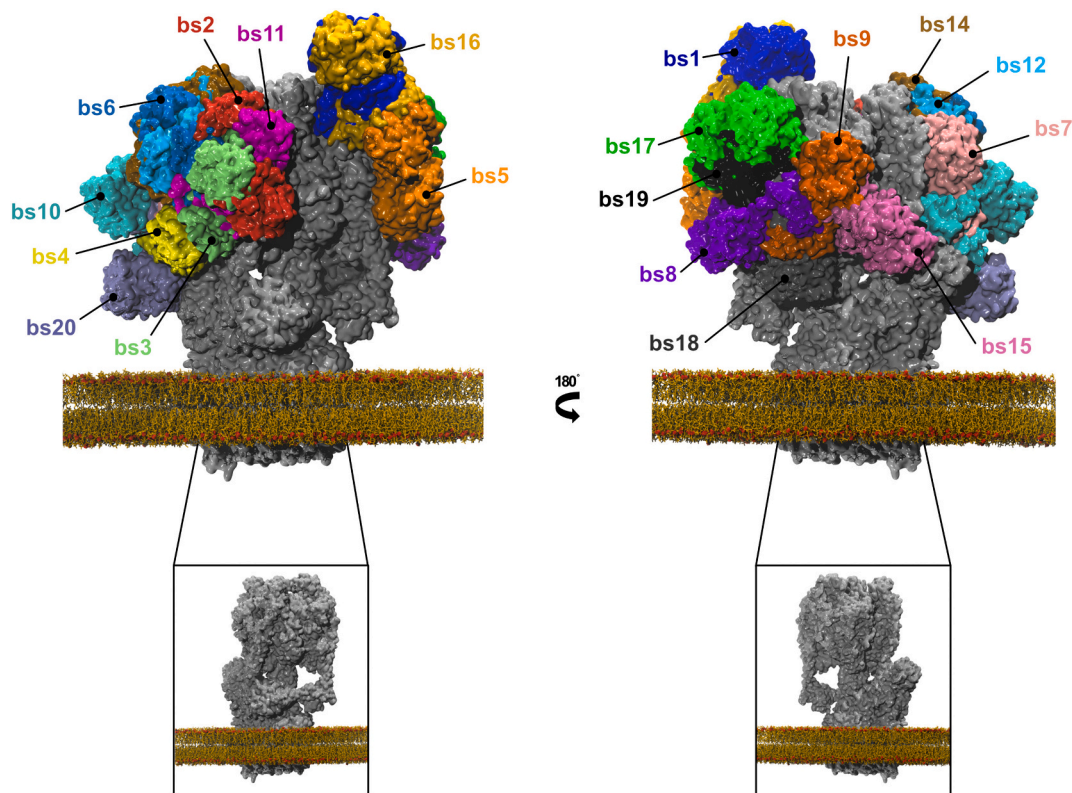


Fig. 4. Docking solutions provided by the HADDOCK software. The top 20 solutions were selected based on the Haddock score and visual analysis, and the 19 solutions that were further analysed are represented. V-ATPase is coloured in white while Lf, which adopts a different binding pose in each solution, is coloured differently according to the solution as labelled. The membrane bilayer used in the MD simulations is also depicted and the following colour scheme was applied: dark yellow for carbon, nitrogen and oxygen and red for phosphate. (For interpretation of the references to colour in this figure legend, the reader is referred to the web version of this article.)

Table 2

Protein-protein docking results. HADDOCK data highlighting the Haddock score, the van der Waals and electrostatic energies, the buried surface area and the V-ATPase subunit to which Lf binds in each docking solution, identified in the first column. bs, best solution; au, arbitrary units.

Complex	Haddock score (au)	van der Waals energy (kcal/mol)	Electrostatic energy (kcal/mol)	Buried surface area (Å ²)	Binding subunit
bs 1	-202.8	-129.5	-711.0	3176	A1, E1
bs 2	-188.9	-92.5	-704.6	3020	A2, E2, G2
bs 3	-183.5	-114.7	-486.6	3535	A2, G3
bs 4	-178.2	-121.8	-354.6	3353	A2, B2, E3, H
bs 5	-176.1	-96.9	-424.7	2723	A1
bs 6	-170.9	-84.9	-478.7	2364	A1, E1
bs 7	-169.3	-83.2	-543.4	2865	A2, B2, E1, G1
bs 8	-164.8	-92.3	-514.8	2496	A3, B3
bs 9	-161.9	-103.7	-450.9	28,812	A3, B3
bs 10	-161.3	-111.2	-319.2	3065	B2, E3, G3, H
bs 11	-158.1	-82.8	-520.7	2756	A2, G2
bs 12	-157.0	-113.2	-296.1	2968	A2, E3
bs 13	-156.4	-88.0	-435.3	2567	A2, E3
bs 14	-156.1	-99.9	-412.6	2617	A2, E3
bs 15	-156.1	-73.9	-456.0	2326	A3
bs 16	-154.6	-98.4	-374.9	2441	A1
bs 17	-153.0	-65.2	-606.7	1733	A3, E1, G1
bs 18	-152.9	-73.9	-370.0	2238	A3, B3
bs 19	-152.8	-93.9	-509.6	2981	B3, E1, G1
bs 20	-151.4	-94.4	-355.6	2369	B2, E3, H

hydrolysis mechanism. Subunits A and B have an overall similar structure that consists of a N-terminal β -barrel domain, a central α/β domain and a C-terminal helical domain. The C-terminal half of A subunits was found to be the responsible for the different conformations of the AB pairs. The nucleotide-binding site is composed by a phosphate-binding loop known as P-loop with the consensus sequence GXXXXGKT(S) (256-263) and Glu 285 and Arg286 both located at the central domain of A subunits. Additionally, an arginine located at the B subunit (the so-called Arg finger) is also involved [70]. Each V-ATPase pump has also three subunits E and G that form three heterodimers. Their major function is to connect the catalytic hexamer to subunits H and C and to the N-terminal domain of a subunit of V_0 domain, connecting in this way ATP hydrolysis to proton transport. They are known as “peripheral stalks” and together with their associated subunits form a stator complex, which ensures that only the central rotor rotates during catalysis, preventing the catalytic subunits and the membrane embedded C-terminal domain of a subunit to turn with the rotor [71].

3.4. Post-docking dynamic refinement of V-ATPase-Lf complexes

Given the well-known limitations of docking scoring functions to predict the protein-protein binding affinity [reviewed by [72]], the docked complexes were further refined and rescored through 25 ns long MD simulations, which provides a dynamic perspective to the protein-protein interactions, and binding free energies calculations (ΔG_{bind}) by the MM-GBSA method. Due to lack of convergence, complex bs13 was discarded at this stage. Before simulations, all the complexes were embedded into a membrane bilayer. This stage allowed structural refinement and quality/reliability assessment of the docking poses. The non-favorable binding poses/interactions would produce unstable trajectories that would reflect significant changes in the RMSD and likely in the SASA values; whereas stable complexes would lead to a constant behaviour after an initial period of system equilibration [73]. All the

docked complexes' MD were equilibrated after the first 15 ns (Fig. S5). In the following 10 ns, the Lf structural behaviour remained stabilized, exhibiting average C α -RMSD values that ranged between 1.7 and 3.4 Å among the different docking solutions (Table 3, 2nd column). Based on the decrease in the Lf solvent accessible area in the complexes MD compared to the MD of Lf alone, the mean area and percentage of Lf buried in each solution was estimated. The buried area varied between 357 and 2281 Å², which corresponds to a percentage of 1.3 to 8.4% of Lf buried (Table 3, 3–5th columns). These data indicates that all the selected solutions form stable complexes, attesting the reliability of our docking approach.

3.5. Binding free energy calculations and detailed analysis of the top four docking solutions

Binding free energy calculations by the MM-GBSA method have been previously shown to approach the experimentally determined binding affinities [74–76]. Rescoring of docking solutions based on these calculations is thus regarded as an excellent strategy to increase the reliability of the final ranking [75,77]. For this reason, the ΔG_{bind} was calculated from the last 10 ns of the complexes MD trajectories. Looking at the overall picture, the analysis of the individual energy terms suggests that electrostatic and, to a lesser extent, van der Waals interactions are the major driving forces for protein-protein binding, which are able to compensate for the observed high penalty in polar solvation energy. In total, with the exception of solution bs19, non-polar energies favor the binding of Lf to V-ATPase over polar ones (Table 4).

Taking into account the total ΔG_{bind} , there are clearly four docking complexes that stand out, owing to their lowest binding free energies: complexes bs3, bs7, bs8 and bs9 (Fig. 5; Table 3, 8th column). Complex bs8 has the lowest ΔG_{bind} (-101.5 ± 2.5 kcal/mol) and a HS of -164.8 , followed by complex bs9 (ΔG : -98.1 ± 1.5 kcal/mol, HS: -161.9), complex bs3 (ΔG : -88.8 ± 2.8 kcal/mol, HS: -183.5) and finally, complex bs7 (ΔG : -81.4 ± 3.0 kcal/mol, HS: -169.3). The next solution with more favorable ΔG_{bind} has more 22.8 kcal/mol, therefore the molecular interactions of these four complexes were subject to a more detailed analysis (Fig. 5B, Table 4). In order to further validate these results, the MD simulations of the top 4 complexes were extended up to 50 ns (Fig. S6A,B) and the MM-GBSA calculations were extended in these simulations to include 600 snapshots. The number of frames used

Table 3

Analysis of the last 10 ns of docked complexes molecular dynamics simulations. The average RMSD, SASA as well as average area and percentage of lactoferrin buried is given in comparison to the molecular dynamics simulation of lactoferrin alone. Values are Å or Å² \pm standard deviation or percentage.

Lf/complex	Average Lf RMSD (Å)	Average Lf SASA (Å ²)	Average Lf buried (Å ²)	Average Lf buried (%)
Lf	2.9 \pm 0.4	27,203 \pm 376	0	0.0
bs 1	1.6 \pm 0.1	24,922 \pm 350	2281 \pm 513	8.4
bs 2	1.7 \pm 0.1	25,671 \pm 397	1531 \pm 546	5.6
bs 3	3.4 \pm 0.2	24,974 \pm 281	2229 \pm 469	8.2
bs 4	1.7 \pm 0.2	25,236 \pm 306	1967 \pm 484	7.2
bs 5	1.6 \pm 0.1	25,886 \pm 240	1317 \pm 446	4.8
bs 6	1.9 \pm 0.2	25,546 \pm 310	1657 \pm 487	6.1
bs 7	2.1 \pm 0.1	25,087 \pm 300	2115 \pm 480	7.8
bs 8	2.0 \pm 0.3	26,223 \pm 263	980 \pm 458	3.6
bs 9	2.0 \pm 0.2	25,132 \pm 277	2071 \pm 467	7.6
bs 10	1.7 \pm 0.1	25,722 \pm 304	1481 \pm 483	5.4
bs 11	2.5 \pm 0.2	26,140 \pm 253	1062 \pm 453	3.9
bs 12	2.0 \pm 0.1	26,813 \pm 337	390 \pm 505	1.4
bs 14	1.7 \pm 0.1	25,837 \pm 260	1366 \pm 457	5.0
bs 15	1.9 \pm 0.3	25,783 \pm 265	1420 \pm 460	5.2
bs 16	2.1 \pm 0.4	26,325 \pm 462	877 \pm 595	3.2
bs 17	2.2 \pm 0.2	26,334 \pm 317	869 \pm 491	3.2
bs 18	2.0 \pm 0.2	25,953 \pm 289	1250 \pm 474	4.6
bs 19	2.2 \pm 0.3	26,846 \pm 369	357 \pm 526	1.3
bs 20	2.2 \pm 0.1	26,100 \pm 309	1103 \pm 484	4.1

Table 4

Binding free energies (ΔG_{bind}) and related energy terms calculated by the MM-GBSA method. Calculations were conducted in 300 structures of the last 10 ns of the docked complexes MD simulations. The polar ΔG is the sum of polar contribution to the solvation free energy (ΔG_{GB}) and electrostatic energies (ΔE_{ELE}), while the non-polar ΔG is the sum of non-polar contribution to the solvation free energy (ΔG_{Surf}) and van der Waals energies (ΔE_{VDW}). The four best solutions based on MM-GBSA calculations that were analysed in more detail in this work are in bold. Values are kcal/mol \pm standard deviation.

Complex	ΔE_{VDW} (kcal/mol)	ΔE_{ELE} (kcal/mol)	ΔG_{GB} (kcal/mol)	ΔG_{Surf} (kcal/mol)	ΔG Non-polar (kcal/mol)	ΔG Polar (kcal/mol)	ΔG_{bind} total (kcal/mol)
bs 1	-134.3 \pm 1.6	-5878.6 \pm 15.0	5987.2 \pm 15.3	-22.0 \pm 0.2	-156.2 \pm 1.8	108.6 \pm 30.3	-47.7 \pm 1.4
bs 2	-126.7 \pm 2.6	-5310.5 \pm 25.2	5448.1 \pm 23.9	-18.7 \pm 0.4	-145.4 \pm 3.0	137.6 \pm 49.0	-7.8 \pm 1.8
bs 3	-197.9 \pm 1.8	-2687.7 \pm 19.4	2827.3 \pm 18.5	-30.4 \pm 0.2	-228.3 \pm 2.0	139.6 \pm 37.9	-88.8 \pm 2.8
bs 4	-161.0 \pm 1.7	-2983.1 \pm 38.8	3144.1 \pm 38.3	-22.6 \pm 0.4	-183.6 \pm 2.1	161.0 \pm 77.0	-22.5 \pm 3.2
bs 5	-155.6 \pm 4.2	-6685.2 \pm 60.4	6804.3 \pm 62.2	-21.1 \pm 0.6	-176.7 \pm 4.8	119.1 \pm 122.6	-57.6 \pm 4.9
bs 6	-85.1 \pm 1.8	-3165.0 \pm 28.7	3214.3 \pm 26.5	-13.0 \pm 0.3	-98.1 \pm 2.1	49.3 \pm 55.2	-48.8 \pm 1.6
bs 7	-180.7 \pm 3.4	-5670.1 \pm 22.2	5800.0 \pm 21.4	-30.6 \pm 0.5	-211.3 \pm 3.9	129.9 \pm 43.6	-81.4 \pm 3.0
bs 8	-111.9 \pm 1.7	-6392.3 \pm 24.3	6422.2 \pm 22.7	-19.4 \pm 0.1	-131.3 \pm 1.9	29.9 \pm 47.0	-101.5 \pm 2.5
bs 9	-129.1 \pm 1.5	-5851.7 \pm 26.6	5903.6 \pm 25.6	-20.9 \pm 0.2	-150.0 \pm 1.7	51.9 \pm 52.5	-98.1 \pm 1.5
bs 10	-153.9 \pm 2.2	-2945.6 \pm 41.1	3086.4 \pm 39.5	-21.0 \pm 0.4	-174.9 \pm 2.6	140.8 \pm 80.7	-34.0 \pm 2.3
bs 11	-177.8 \pm 2.4	-2817.4 \pm 26.9	2981.9 \pm 27.7	-23.7 \pm 0.4	-201.4 \pm 2.8	164.4 \pm 54.7	-36.9 \pm 1.9
bs 12	-97.5 \pm 1.4	-3745.0 \pm 20.1	3832.7 \pm 20.1	-14.2 \pm 0.2	-111.6 \pm 1.6	87.7 \pm 40.2	-23.9 \pm 1.1
bs 14	-143.5 \pm 2.4	-2698.2 \pm 39.7	2833.1 \pm 39.9	-19.2 \pm 0.4	-162.7 \pm 2.8	134.9 \pm 79.6	-27.8 \pm 2.3
bs 15	-129.3 \pm 1.9	-4784.6 \pm 29.3	4877.8 \pm 27.3	-21.2 \pm 0.3	-150.6 \pm 2.2	93.2 \pm 56.7	-57.4 \pm 3.0
bs 16	-114.4 \pm 2.6	-5830.9 \pm 62.5	5904.4 \pm 60.8	-17.7 \pm 0.6	-132.1 \pm 3.2	73.5 \pm 123.3	-58.6 \pm 4.8
bs 17	-80.1 \pm 1.3	-5481.4 \pm 27.4	5533.3 \pm 26.7	-12.7 \pm 0.1	-92.7 \pm 1.4	51.9 \pm 54.1	-40.2 \pm 1.7
bs 18	-135.1 \pm 2.6	-2863.2 \pm 23.8	2968.1 \pm 23.5	-19.4 \pm 0.4	-154.5 \pm 3.0	104.9 \pm 47.3	-49.5 \pm 2.9
bs 19	-106.7 \pm 2.5	-4013.3 \pm 27.8	4144.3 \pm 26.9	-15.6 \pm 0.4	-122.2 \pm 2.9	131.0 \pm 54.7	8.7 \pm 2.9
bs 20	-99.6 \pm 3.5	-2577.1 \pm 26.3	2668.5 \pm 27.5	-13.0 \pm 0.4	-112.6 \pm 3.9	91.4 \pm 53.8	-21.2 \pm 2.8

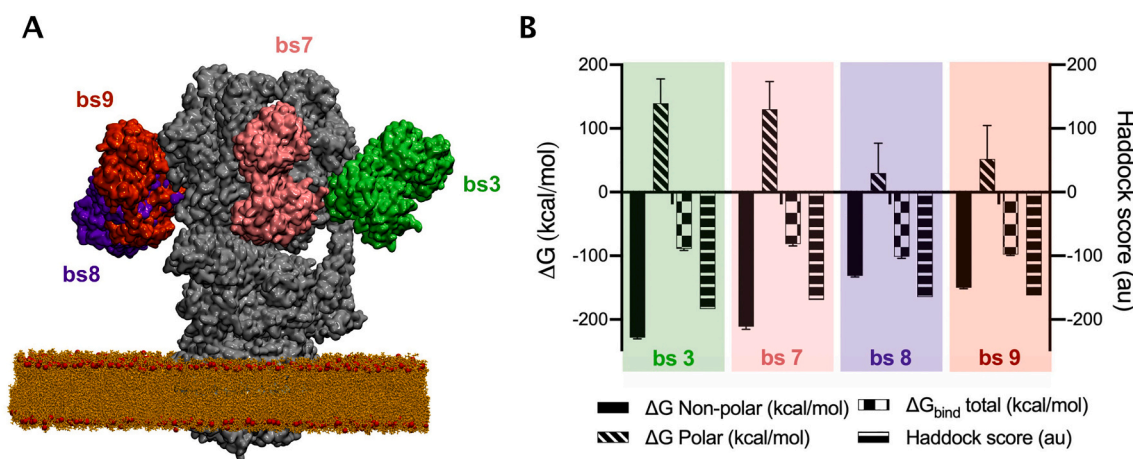


Fig. 5. Global analysis of the top four solutions. (A) Visual representation of the docking poses of the top four solutions (bs3, bs7, bs8 and bs9). V-ATPase is coloured in gray whereas Lf is coloured differently according to the docking pose. A snapshot of the lipid bilayer is also represented. The following colour scheme was applied: dark yellow for carbon, nitrogen and oxygen and red for phosphate. Water molecules are omitted for clarity. (B) Comparison between total, polar and non-polar binding free energies calculated by the MM-GBSA method as well as Haddock score for the best four solutions. au, arbitrary units. (For interpretation of the references to colour in this figure legend, the reader is referred to the web version of this article.)

is in accordance with other recent MM-GBSA applications [78–81]. Results obtained with the extended MM-GBSA analysis were perfectly in line with the previous ones since very similar ΔG_{bind} values were obtained and the same ranking of the complexes was attained. Similarly to the 25 ns simulations, non-polar contribution favors the proteins' binding (Fig. S6C).

To identify the residues of both proteins, as well as the interactions critical for the protein-protein binding, energy per-residue decomposition analysis was performed also using the MM-GBSA approach. This analysis allows the calculation of the energetic contribution of the individual amino acids to the total free energy. Fig. S7 shows the free binding energy of the three V-ATPase residues with higher contribution to the binding in each complex. Naturally, the residues belong to the subunits already identified (Table 2) as the Lf-binding subunits in each complex (subunits A, B, E, G and H). However, with this analysis, a finer level is achieved as the most contributing residues of each particular subunit are identified. Importantly, about 49% of the residues belong to subunits A and 28% to subunits B, which are the V-ATPase nucleotide

binding subunits.

Focusing on the top four docking solutions (Fig. 6, Movies S2–S5), in complexes bs8 and bs9, which have the lowest ΔG_{bind} , Lf binds to the interface between subunits A3 and B3 through its highly cationic N-terminal lobe (N-lobe). In complex bs3, Lf binds, once again through its N-lobe, in the interface between subunit A2 and G3, and finally, in complex bs7, both Lf lobes bind to the interface between subunits A2 and B2, as well as to the interface between subunit B2 with subunits E1 and G1 (Fig. 6, Movies S2–S5).

Based on the decomposition data and visual inspection, the atomistic interaction spectra for the top four docking complexes were scrutinized (Table 5, Movies S2–S5). Several salt bridges/ionic networks between the sidechains of oppositely charged amino acids (Asp, Glu vs Arg, Lys) connected with several hydrogen bonds can be observed in all complexes. Salt bridges are among the strongest non-covalent interactions, contributing to a strong binding between molecules. This, together with the observed high number of amino acidic interactions (Table 5), is perfectly aligned with the very favorable free binding energies

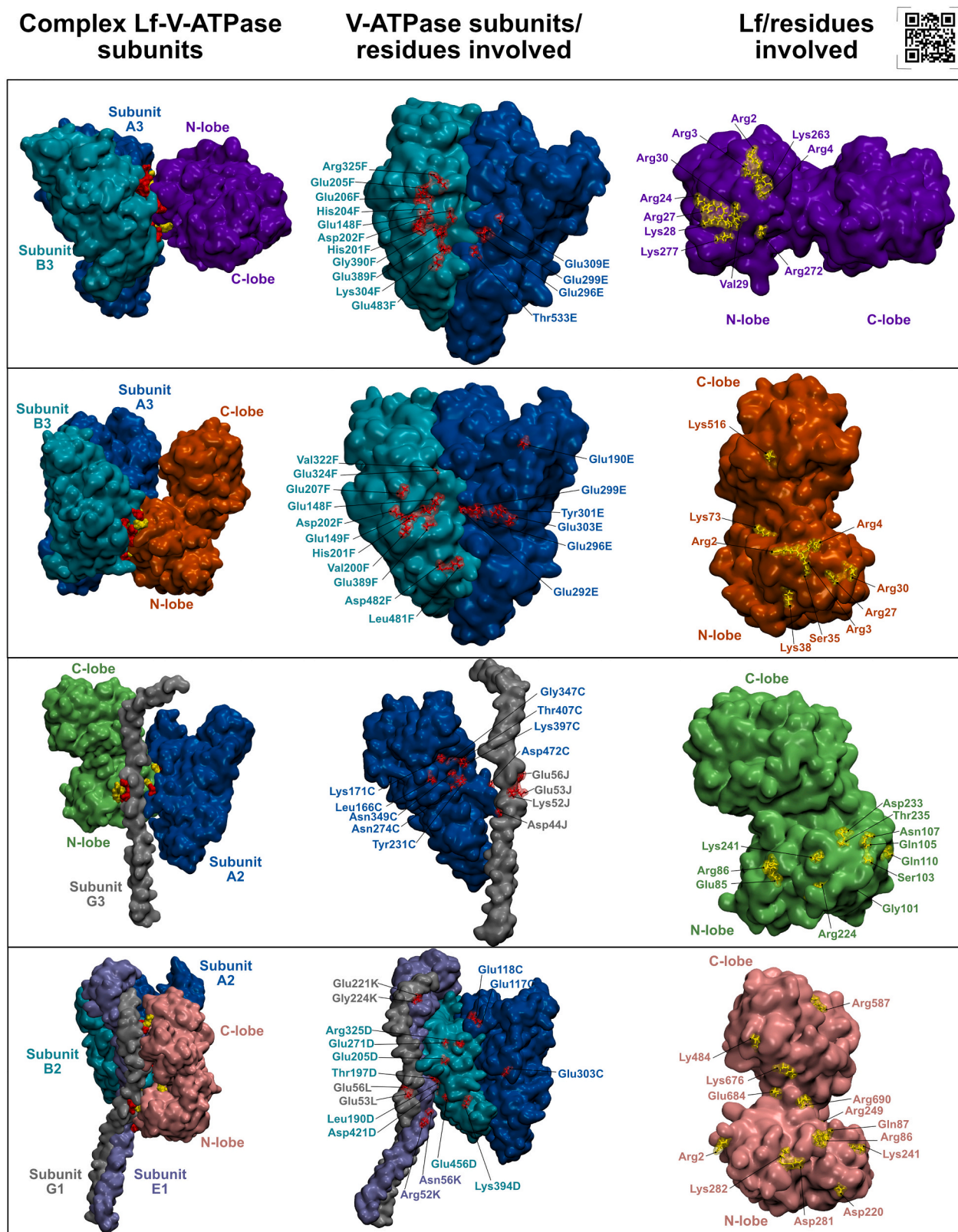


Fig. 6. Identification of the critical interacting subunits and most important residues in the top four docking solutions. Lactoferrin is coloured in purple, orange, green or pink depending on the docked complex. Subunits A are coloured in blue, subunits B in cyan, subunits G in gray and subunit E1 in lilac. On the left, the Lf binding poses in each docking complex as well as the binding V-ATPase subunits are depicted. The interacting residues of Lf and V-ATPase are coloured in yellow and red, respectively. The Lf N- or C-terminal lobes (N- or C-lobe) are also identified. On the right, the interacting residues identified by both the decomposition analysis by the MM-GBSA method and visual inspection of the interaction maps, are labelled according to the colour of the respective location. Interactive view QR code: <https://biosim.pt/lactoferrin/>. (For interpretation of the references to colour in this figure legend, the reader is referred to the web version of this article.)

Table 5
Interactions formed between lactoferrin and V-ATPase in the top four docking solutions. The type of bond formed between the different amino acid pairs is indicated as HB for hydrogen bonds and SB for salt bridges. Moreover, for each residue, it is indicated whether the bond is through its sidechain functional group (s) or its backbone (b) group. The letter after the number in V-ATPase residues corresponds to the chain to which the residue belongs. The information regarding the V-ATPase subunit is also depicted.

Lf residue	V-ATPase residue	V-ATPase subunit	Bond type	Lf residue	V-ATPase residue	V-ATPase subunit	Bond type	Lf residue	V-ATPase residue	V-ATPase subunit	Bond type	Lf residue	V-ATPase residue	V-ATPase subunit	Bond type
bs 3				bs 7				bs 8				bs 9			
Glu85 (s)	Lys52J (s)	G3	SB	Arg2 (s)	Glu303C (s)	A2	SB	Arg2 (s)	Glu205F (s)	B3	SB	Arg2 (s)	Glu292E (s)	A3	SB
Arg86 (s)	Glu56J (s)	G3	SB	Arg86 (s)	Leu190D (b)	B2	HB	Arg3 (s)	Glu206F (s)	B3	SB		Glu296E (s)	A3	SB
	Glu53J (s)	G3	SB		Asp421D (s)	B2	SB		Arg325F (b)	B3	HB		Glu299E (s)	A3	SB
Gly101 (b)	Tyr231C (s)	A2	HB		Glu456D (s)	B2	SB	Arg4 (s)	Asp199F (s)	B3	SB	Arg3 (s)	Glu389F (s)	B3	SB
Ser103 (s)	Asn274C (b)	A2	HB	Gln87 (s)	Thr197D (s)	B2	HB		Asp199F (b)	B3	HB		Glu148F (b)	B3	HB
Ser103 (b)	Asn274C (b)	A2	HB	Asp220 (s)	Arg52K (s)	E1	SB		His201F (b)	B3	HB	Arg4 (s)	Glu148F (s)	B3	SB
Gln105 (s)	Asn349C (s)	A2	HB	Lys241 (s)	Asn56K (s)	E1	HB	Arg4 (b)	Gly390F (b)	B3	HB		Glu148F (b)	B3	HB
Asn107 (s)	Thr407C (b)	A2	HB		Glu53L (s)	G1	SB		His204F (s)	B3	HB		Val322F (b)	B3	HB
Asn107 (b)	Gly347C (b)	A2	HB		Glu56L (s)	G1	SB	Arg24 (s)	Glu309E (s)	A3	SB		Gly324F (b)	B3	HB
Gln110 (s)	Lys171C (s)	A2	HB	Arg249 (s)	Asp202D (s)	B2	SB	Arg27 (s)	Glu296E (s)	A3	SB	Arg27 (s)	Glu149F (s)	B3	SB
Arg224 (s)	Leu166C (b)	A2	HB	Asp281 (b)	Lys394D (b)	B2	HB		Glu299E (s)	A3	SB		Val200F (b)	B3	HB
Asp233 (b)	Asp44J (s)	G3	SB	Ser482 (s)	Glu117C (b)	A2	HB	Lys28 (s)	Glu296E (s)	A3	SB		His201F (b)	B3	HB
Thr235 (s)	Thr407C (b)	A2	HB	Lys484 (s)	Glu118C (s)	A2	SB		Glu299E (s)	A3	SB		Asp202F (b)	B3	HB
Lys241 (s)	Thr407C (s)	A2	HB	Arg587 (s)	Glu221K (s)	E1	SB	Val29 (b)	Lys394F (s)	B3	HB	Arg30 (s)	Glu205F (s)	B3	SB
	Lys397C (s)	A2	HB		Gly224K (s)	E1	SB	Arg30 (s)	Glu148F (b)	B3	HB		Asp202F (s)	B3	SB
	Asp472C (s)	A2	SB	Lys676 (s)	Glu271D (s)	B2	SB		Gly388F (b)	B3	HB	Ser35 (s)	Glu389F (s)	B3	HB
				Arg690 (s)	Glu205D (s)	B2	SB		Glu389F (b)	B3	HB	Lys38 (s)	Leu481F (b)	B3	HB
				Glu684 (s)	Arg325D (s)	B2	SB	Lys263 (s)	Asp202F (s)	B3	SB		Asp482F (s)	B3	SB
								Arg272 (s)	Glu483F (s)	B3	SB	Lys73 (s)	Glu303F (s)	A3	SB
								Lys277 (s)	Thr533E (s)	A3	HB		Tyr301F (s)	A3	HB
												Lys516 (s)	Glu190F (s)	A3	SB

calculated by the MM-GBSA method (ranging from -101.5 ± 2.5 to -81.4 ± 3.0) for these complexes. The network includes single, as well as complex salt bridges that join more than two charged residues. In complex bs3, Lf and V-ATPase interact through a salt bridge triad Glu56J-Arg86-Glu53J, as well as 3 single salt bridges (Glu85-Lys52J, Arg224-Asp44J and Lys241-Asp472C). A network of 11 hydrogen bonds mainly involving polar amino acids further strengthens the proteins interaction. In complexes bs7, bs8 and bs9 a strong salt bridge network generally between the positively charged residues from Lf (Arg, Lys) and the negatively charged amino acids from V-ATPase subunits A, B, E and G (Glu, Asp) characterizes the interaction between the two proteins. In bs7, 7 single and 5 complex salt bridges were identified, 6 single and 2 complex in bs8, and 5 single and 2 complex in bs9. Several backbone and sidechain hydrogen bonds involving both charged and polar residues are also present and reinforce the protein-protein interaction (5 in bs7, 9 in bs8 and 10 in bs9) (Table 5).

3.6. Identification of critical V-ATPase and lactoferrin binding residues and insights for future experimental studies

The free energy decomposition study allowed us to gather a detailed atomistic analysis of the V-ATPase-Lf interactions in the different docked complexes affording the identification of some important protein-protein interaction patterns. Indeed, by performing an overall analysis of the residues with more favorable free binding energies that appear in more than one docking solution (Fig. 7), several residues belonging to particular regions of both proteins were identified as those that mainly contribute to the binding in several complexes, which constitute prime candidates for future experimental work.

Almost all the Lf residues with a maximum contribution to the total free binding energy below -8 kcal/mol that appear in more than one solution are arginine residues with the exception of Gln666 (Fig. 7A, B). Noticeably, three consecutive N-terminal arginine residues at positions 2–4 together with Arg27, which locates nearby, form a highly cationic N-terminal stretch that seems to be involved in the binding of different complexes as it can be observed in Fig. 5 for the top two solutions (bs8 and bs9). These residues exhibit a maximum contribution to the total ΔG_{bind} below -10 kcal/mol and appear in more than 3 solutions (Fig. 7A), being thus excellent candidates for mutagenesis studies. In accordance, they are involved in different single and complex salt bridges with the negatively charged amino acids from V-ATPase (Table 5). Three additional arginine residues also located at the Lf N-lobe (Arg86, Arg89 and Arg249) also display highly favorable ΔG (below -8 kcal/mol). A special remark to Arg86 that appears as an important binding residue in 8 of 19 solutions with a maximum contribution below -10 kcal/mol and that forms salt bridge triads with aspartates and glutamates from V-ATPase in solutions bs3 and bs7 (Table 5). In fact, due to its highly cationic nature, the N-terminal part of Lf has been suggested to be responsible for the binding of Lf to a wide collection of molecules and to be the source of strong antimicrobial peptides [6]. In accordance with our results, two clusters composed by the first 6 Lf amino acids (GRRRRS) and RKVR residues located at positions 28–31 were previously identified to be the Lf binding site for some glycosaminoglycans (GAGs) including chondroitin sulfate [82] and heparin [83]. The positively charged sidechains of the residues belonging to these two clusters, which are juxtaposed in the folded protein, were suggested to form a “cationic cradle” for the GAGs binding [83]. Residues belonging to these clusters were also found to be important for the binding of the pneumococcal surface protein A from *Streptococcus pneumoniae* [84]. Residues 28–34 from hLf and the homologous region of bLf were also demonstrated to be important for the binding of human to lipopolysaccharide (LPS), playing thus an important role in Lf-driven host defense, particularly against Gram-negative bacteria [85]. At the Lf C-lobe, three arginine residues (Arg587, Arg608 and Arg652) as well as Gln666 appear as important interactors in two or three docking solutions and exhibit maximum contribution

below 8 kcal/mol. It is clear though from these data that the N-terminal Lf lobe is enriched in residues that appear in more than one solution and exhibit maximum contribution to the total ΔG below -4 kcal/mol (Fig. 7A, B). The Lf C-lobe has previously been implicated in the binding to different molecules including the Lf-binding proteins A and B from Gram-negative bacteria [86,87] and some anti-inflammatory drugs [88]. It is worth mentioning that three different drugs were found to bind to the same ligand-binding site at the Lf C-lobe [88] that are near the Arg652 and Gln666 identified in our study. Additionally, the same Lf region was found to be a binding pocket for different sugars including glucose, galactose, mannose and xylose [89]. Our results are thus in line with published work, which attests the reliability of our computational pipeline.

The V-ATPase portrait of residues that display a maximum contribution to the total ΔG below -2 kcal/mol and appear in more than one docking complex is enriched in charged residues. As for their location, the great majority belong to subunits A and B (38% and 41%, respectively), 15% to subunit E and only 1 residue to subunits G and H (Fig. 7C). Looking at the overall picture and focusing on those with ΔG below -5 kcal/mol, a group of four negatively charged amino acids (Glu149F, Asp199F, Glu206F and Glu389F) together with Arg466F and Phe484F located at subunit B3 immediately grabs our attention (Fig. 7D). Some of those are involved in strong salt bridges with the positively charged residues from Lf in the top four solutions (Table 5). Subunit B3 comprises the only three residues with maximum contribution below -8 kcal/mol that appear in more than one solution (Glu206F, Glu389F and Arg466F) (Fig. 7C, D) and is involved in the binding to Lf in the top two solutions (Fig. 6). Site-directed mutagenesis studies targeting these residues, as well as deletion of subunit B are thus promising approaches that can be further explored experimentally. Residues Ser165C, Leu166A and Glu296E from subunits A, as well as Asp44L from subunit G and Arg52K from subunit E also display a particularly favorable maximum contribution to the total ΔG (Fig. 7C, D) and participate in salt bridges in the top four solutions (Table 5).

In summary, our energy decomposition study by the MM-GBSA method allowed the identification of critical Lf and V-ATPase residues that can greatly aid in the rational design of experimental studies.

Considering the overall docking results, Lf binds to subunits A, which hold the nucleotide binding sites, in 85% of the solutions, suggesting that the most probable mechanism through which Lf inhibits V-ATPase activity is by interfering with the hydrolysis mechanism (Fig. 8). Accordingly, in three of the four top solutions, Lf establishes a strong interaction map that counts with several single and complex salt bridges, as well as a hydrogen bond network with the central α/β domain of the ATP-hydrolyzing interfaces of the AB pairs (where the key residues for nucleotide binding are located), reinforcing our hypothesis. By binding to the AB interfaces, Lf may (i) inhibit ATP binding by a competitive mechanism or by (ii) limiting the accessibility of ATP to the catalytic sites. Moreover, its binding may (iii) impair the conformational changes of the AB pairs required to continue the rotational reaction after the ATP hydrolysis and ADP release [90]. To try to clarify these hypotheses, we performed an alignment of the four best solutions with the 6WM2 structure of V-ATPase that has ADP on the active site. In Fig. S8, it is clear that, in three of the four top complexes, Lf blocks the active site of V-ATPase located between subunits A and B, which would prevent ATP from accessing the active center or ADP from exiting. Moreover, this binding is likely to hinder the conformational changes required for catalysis. Therefore, based on these data, hypotheses (ii) and (iii) are the most probable explanation for the Lf-induced V-ATPase inhibition. Depending on the docking solution, Lf binds to either AB pair 1, 2 or 3. Therefore, similarly to the bacterial effector SidK from *Legionella pneumophila* [91], different Lf proteins may bind to the same V-ATPase complex further boosting the inhibitory activity. Indeed, the V-ATPase-SidK complexes were determined by cryo-EM and showed that three SidK molecules bound to the three A subunits reducing their flexibility in both yeast and human [46,91]. Complementary in vitro experiments

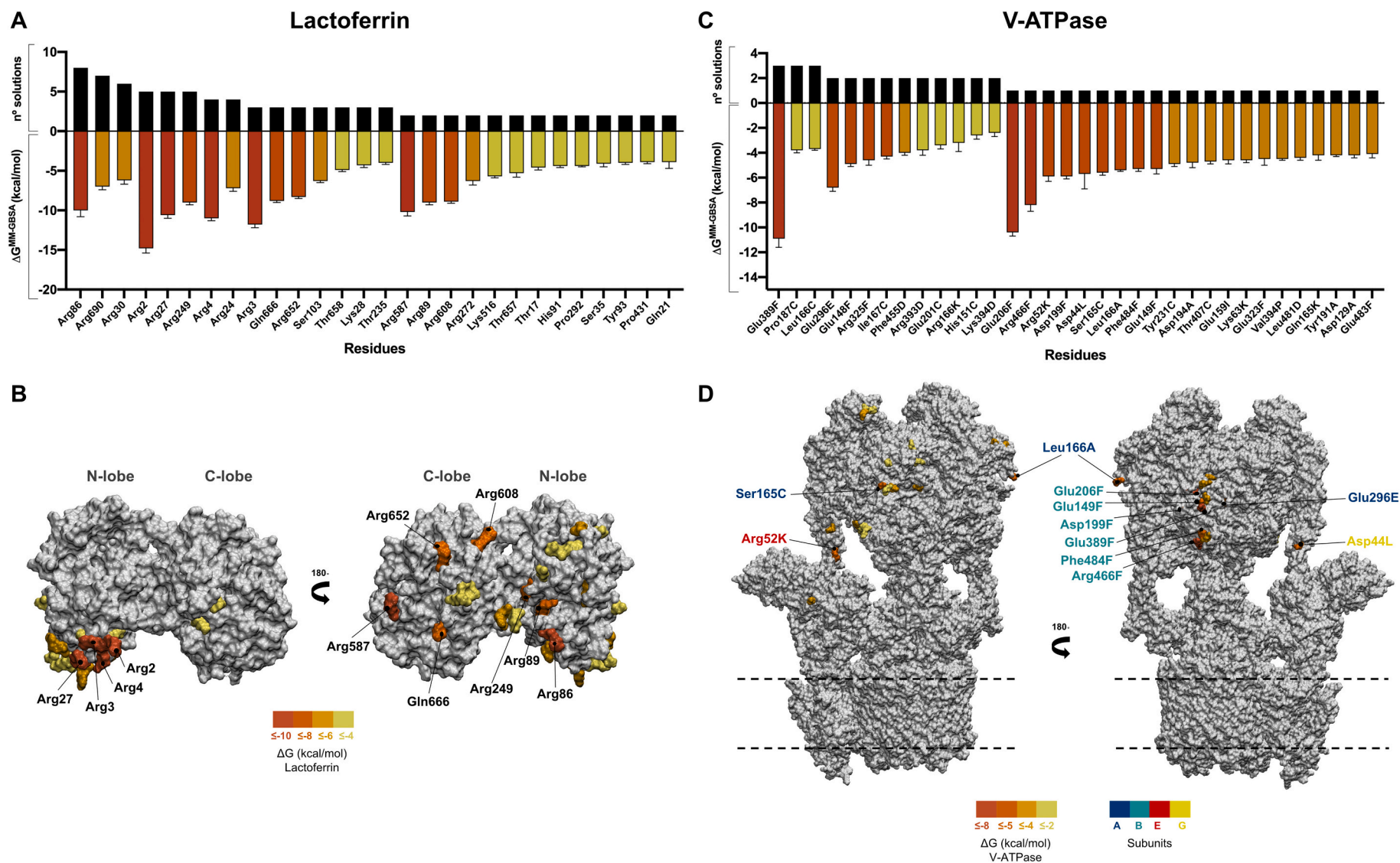


Fig. 7. General analysis of the critical lactoferrin and V-ATPase binding residues based on the decomposition of the binding free energy calculated using the MM-GBSA method. (A) Per-residue ΔG in kcal/mol of the lactoferrin amino acids with maximum contribution to the total free binding energy below -4 kcal/mol that appear in more than one docking solution as important binding residues. The number of solutions is indicated in the positive part of the y-axis while the ΔG is depicted in the negative portion. (B) Surface model of lactoferrin (in white) showing the location of the residues with maximum contribution below -4 kcal/mol. Four different categories were defined based on residues ΔG (below -10 , -8 , -6 and -4 kcal/mol) that are coloured differently as indicated in the colour legend. The names of the residues with ΔG below -8 kcal/mol are depicted. (C) Same as in A but representing the V-ATPase residues with maximum contribution to the total binding free energy below -2 kcal/mol. (D) Surface model of V-ATPase (in white) showing the location of the residues with maximum contribution below -2 kcal/mol. Four different categories were defined based on residues ΔG (below -8 , -5 , -4 and -2 kcal/mol) that are coloured differently as indicated in the colour legend. The residues with ΔG below -5 kcal/mol are labelled with the letting colour according to the V-ATPase subunit they belong as indicated. The dashed lines indicate the approximate location of the membrane. (For interpretation of the references to colour in this figure legend, the reader is referred to the web version of this article.)

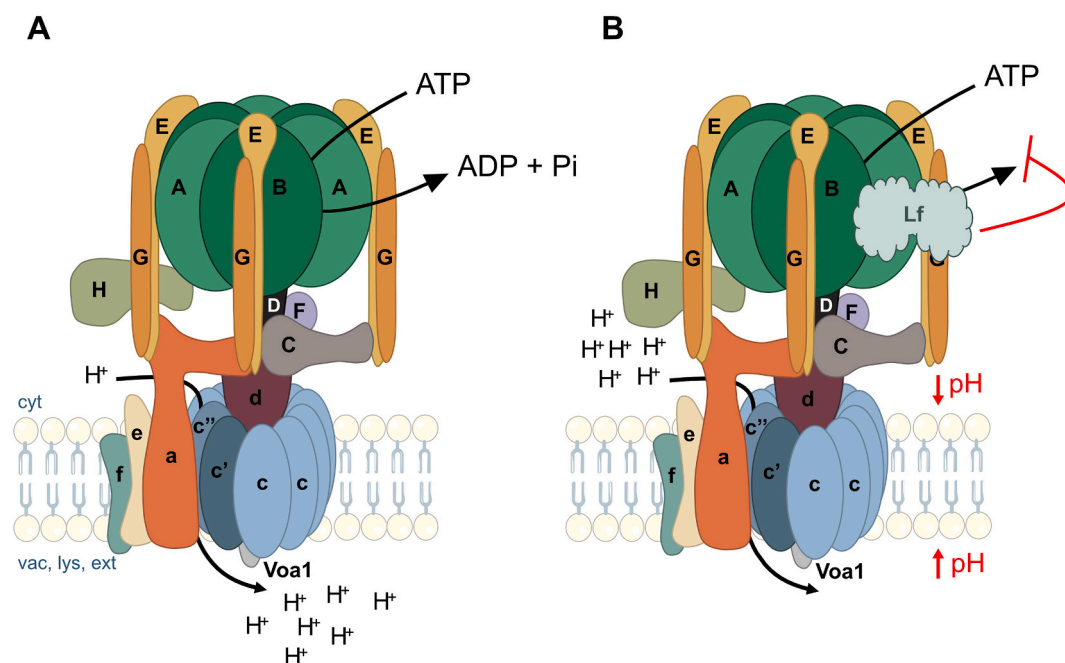


Fig. 8. Working model of the mode of V-ATPase inhibition by lactoferrin. (A) In physiological conditions, V-ATPase located either at the vacuolar, lysosomal or plasma membrane couples the energy of ATP hydrolysis to pump protons from the cytosol (cyt) to the vacuolar (vac) or lysosomal lumen (lys) or to the extracellular milieu (ext). (B) In the presence of Lf, it binds to the interface between the V-ATPase AB pairs, hindering ATP hydrolysis which, in turn, inhibits proton translocation, leading to intracellular acidification and organelle/extracellular space alkalinization.

revealed that SidK reduces V-ATPase activity and decreases its affinity for ATP [91]. In another study, the insecticidal compound celangulin V was shown to inhibit ATP hydrolysis and, by a docking approach, suggested to bind to the ATP binding site of the AB subunits [92].

4. Conclusion

Based on all the aforementioned evidence, we hypothesize that Lf targets the AB pairs, hindering ATP hydrolysis by binding to their interfaces and blocking the catalytic site, which, in turn, impairs proton transport and the overall V-ATPase activity (Fig. 8). In agreement with this model, in our previous work, we demonstrated that Lf inhibits both the hydrolytic and proton pumping activities of V-ATPase in lysosomes isolated from rat liver [7], and its proton pumping activity in vacuoles isolated from yeast [9]. In the future, it would be interesting to study the Lf effect on the V-ATPase hydrolytic activity in vacuoles isolated from yeast. This Lf inhibitory activity towards V-ATPase culminates in lethal pH perturbations in both yeast [9] and highly metastatic cancer cells [7,8], as discussed in the Introduction section.

The computational strategy used in this work identified the V_1 domain of V-ATPase as a Lf target, and allowed us to infer upon the molecular basis of Lf-driven V-ATPase inhibition and to propose key binding residues from both proteins that can be explored experimentally. Taking into account our results and the fact that Lf was also shown to inhibit the bacterial F-ATPase [93], which is functionally and structurally similar to V-ATPase [94], a comparable mechanism may be involved in the F-ATPase inhibition by Lf and may underlie the antibacterial activity of this protein. Indeed, ATP hydrolysis in F-ATPases occurs in the catalytic hexamer $\alpha_3\beta_3$ (A_3B_3 in V-ATPase) [94], which can be a putative Lf target in bacteria.

Supplementary data to this article can be found online at <https://doi.org/10.1016/j.ijbiomac.2021.06.200>.

Funding

This work was supported by national funds from the Portuguese

Foundation for Science and Technology (FCT) under the scope of the strategic funding UIDP/04378/2020, UIDB/04378/2020, UIDB/04469/2020 and UIDB/04050/2020; and by the BioTecNorte operation (NORTE-01-0145-FEDER-000004) funded by the European Regional Development Fund under the scope of Norte2020 - Programa Operacional Regional do Norte. Cátia Santos-Pereira acknowledges the PhD fellowship PD/BD/128032/2016 funded by FCT under the scope of the doctoral program in Applied and Environmental Microbiology (DP.AEM). Juliana F. Rocha is the recipient of the SFRH/BD/136746/2018 fellowship supported by FCT. Henrique S. Fernandes acknowledges FCT for his Ph.D. grant SFRH/BD/115396/2016. Some of the calculations were produced with the support of INCDC funded by FCT and FEDER under the project 01/SAICT/2016 number 022153.

CRediT authorship contribution statement

Cátia Santos Pereira: Conceptualization, Data curation, Formal analysis, Investigation, Validation, Visualization, Writing - original draft, Writing - review & editing; **Juliana F. Rocha and Henrique S. Fernandes:** Data curation, Formal analysis, Validation, Visualization, Writing - review & editing; **Lígia R. Rodrigues, Manuela Côrte-Real and Sérgio F. Sousa:** Conceptualization, Data curation, Funding acquisition, Project administration, Resources, Supervision, Validation, Writing - review & editing.

Declaration of competing interest

The authors declare no competing interests.

References

- [1] B. Wang, Y.P. Timilsena, E. Blanch, B. Adhikari, Lactoferrin: Structure, function, denaturation and digestion, *Crit. Rev. Food Sci. Nutr.* 59 (2019) 580–596, <https://doi.org/10.1080/10408398.2017.1381583>.
- [2] B.F. Anderson, H.M. Baker, E.J. Dodson, G.E. Norris, S.V. Rumball, J.M. Waters, E. N. Baker, Structure of human lactoferrin at 3.2-Å resolution, *Proc. Natl. Acad. Sci. U. S. A.* 84 (1987) 1769–1773, <https://doi.org/10.1073/pnas.84.7.1769>.

- [3] S.A. Moore, B.F. Anderson, C.R. Groom, M. Haridas, E.N. Baker, Three-dimensional structure of diferric bovine lactoferrin at 2.8 Å resolution, *J. Mol. Biol.* 274 (1997) 222–236, <https://doi.org/10.1006/jmbi.1997.1386>.
- [4] A. Pierce, D. Colavizza, M. Benaissa, P. Maes, A. Tartar, J. Montreuil, G. Spik, Molecular cloning and sequence analysis of bovine lactotransferrin, *Eur. J. Biochem.* 196 (1991) 177–184, <https://doi.org/10.1111/j.1432-1033.1991.tb15801.x>.
- [5] H.M. Baker, E.N. Baker, A structural perspective on lactoferrin function, *Biochem. Cell Biol.* 90 (2012) 320–328, <https://doi.org/10.1139/o11-071>.
- [6] D. Zarzosa-Moreno, C. Avalos-Gómez, L. Ramírez-Textcalco, E. Torres-López, R. Ramírez-Mondragón, J. Hernández-Ramírez, J. Serrano-Luna, M. de la Garza, Lactoferrin and its derived peptides: an alternative for combating virulence mechanisms developed by pathogens, *Molecules* 25 (2020) 5763, <https://doi.org/10.3390/molecules25245763>.
- [7] C.S. Pereira, J.P. Guedes, M. Gonçalves, L. Loureiro, L. Castro, H. Gerós, L. R. Rodrigues, M. Côte-Real, Lactoferrin selectively triggers apoptosis in highly metastatic breast cancer cells through inhibition of plasmalemmal V-H-ATPase, *Oncotarget* 7 (2016) 62144–62158, <https://doi.org/10.18632/oncotarget.11394>.
- [8] J. Guedes, C. Pereira, L. Rodrigues, M. Côte-real, Bovine milk lactoferrin selectively kills highly metastatic prostate cancer PC-3 and osteosarcoma MG-63 cells in vitro, *Front. Oncol.* 8 (2018) 1–12, <https://doi.org/10.3389/fonc.2018.00200>.
- [9] C. Santos-Pereira, M.T. Andrés, S.R. Chaves, J.F. Fierro, H. Gerós, S. Manon, L. R. Rodrigues, M. Côte-Real, Lactoferrin perturbs lipid rafts and requires integrity of Pma1p-lipid rafts association to exert its antifungal activity against *Saccharomyces cerevisiae*, *Int. J. Biol. Macromol.* 171 (2021) 343–357, <https://doi.org/10.1016/j.ijbiomac.2020.12.224>.
- [10] M.A. Harrison, S.P. Muench, The vacuolar ATPase – a nano-scale motor that drives cell biology, *Subcell. Biochem.* 87 (2018) 409–459, https://doi.org/10.1007/978-981-10-7757-9_14.
- [11] J. Zhao, S. Benlekber, J.L. Rubinstein, Electron cryomicroscopy observation of rotational states in a eukaryotic V-ATPase, *Nature* 521 (2015) 241–245, <https://doi.org/10.1038/nature14365>.
- [12] S.H. Roh, M. Shekhar, G. Pintlilie, C. Chipot, S. Wilkens, A. Singharoy, W. Chiu, Cryo-EM and MD infer water-mediated proton transport and autoinhibition mechanisms of Vo complex, *Sci. Adv.* 6 (2020) 1–10, <https://doi.org/10.1126/sciadv.abb9605>.
- [13] R.A. Oot, S. Couoh-Cardel, S. Sharma, N.J. Stam, S. Wilkens, Breaking up and making up: the secret life of the vacuolar H-ATPase, *Protein Sci.* 26 (2017) 896–909, <https://doi.org/10.1002/pro>.
- [14] M.T. Mazhab-Jafari, A. Rohou, C. Schmidt, S.A. Bueler, S. Benlekber, C. V. Robinson, J.L. Rubinstein, Atomic model for the membrane-embedded Vo motor of a eukaryotic V-ATPase, *Nature* 539 (2016) 118–122, <https://doi.org/10.1038/nature19828>.
- [15] C. Santos-Pereira, L.R. Rodrigues, M. Côte-Real, Emerging insights on the role of V-ATPase in human diseases: therapeutic challenges and opportunities, *Med. Res. Rev.* (2021) 1–38, <https://doi.org/10.1002/med.21782>.
- [16] M. Acosta-Zaldívar, M.T. Andrés, A. Rego, C.S. Pereira, J.F. Fierro, M. Côte-Real, Human lactoferrin triggers a mitochondrial- and caspase-dependent regulated cell death in *Saccharomyces cerevisiae*, *Apoptosis* 21 (2016) 163–173, <https://doi.org/10.1007/s10495-015-1199-9>.
- [17] S.F. Sousa, A.J.M. Ribeiro, J.T.S. Coimbra, R.P.P. Neves, S.A. Martins, N.S.H. N. Moorthy, P.A. Fernandes, M.J. Ramos, Protein-ligand docking in the new millennium – a retrospective of 10 years in the field, *Curr. Med. Chem.* 20 (2013) 2296–2314, <https://doi.org/10.2174/0929867311320180002>.
- [18] A.J. Preto, P. Matos-Filipe, P.I. Koukos, P. Renault, S.F. Sousa, I.S. Moreira, Structural Characterization of Membrane Protein Dimers, 2019, https://doi.org/10.1007/978-1-4939-9161-7_21.
- [19] S.J. De Vries, M. Van Dijk, A.M.J.J. Bonvin, The HADDOCK web server for data-driven biomolecular docking, *Nat. Protoc.* 5 (2010) 883–897, <https://doi.org/10.1038/nprot.2010.32>.
- [20] A. Onufriev, D. Bashford, D.A. Case, Exploring protein native states and large-scale conformational changes with a modified generalized born model, *Proteins Struct. Funct. Genet.* 55 (2004) 383–394, <https://doi.org/10.1002/prot.20033>.
- [21] M. Haridas, B.F. Anderson, E.N. Baker, Structure of human diferric lactoferrin refined at 2.2 Å resolution, *Acta Crystallogr. Sect. D: Biol. Crystallogr.* 51 (1995) 629–646, <https://doi.org/10.1107/S0907444994013521>.
- [22] M.H.M. Olsson, C.R. Søndergaard, M. Rostkowski, J.H. Jensen, PROPKA3: consistent treatment of internal and surface residues in empirical pK_a predictions, *J. Chem. Theory Comput.* 7 (2011) 525–537, <https://doi.org/10.1021/ct100578z>.
- [23] L. Anghele, A. Radulescu, R.V. Erhan, Structural aspects of human lactoferrin in the iron-binding process studied by molecular dynamics and small-angle neutron scattering, *Eur. Phys. J. E.* 41 (2018), <https://doi.org/10.1140/epje/i2018-11720-x>.
- [24] P. Li, K.M. Merz, MCPB.py: a python based metal center parameter builder, *J. Chem. Inf. Model.* 56 (2016) 599–604, <https://doi.org/10.1021/acs.jcim.5b00674>.
- [25] M. Frisch, G. Trucks, H. Schlegel, G. Scuseria, M. Robb, J. Cheeseman, G. Scalmani, V. Barone, G. Petersson, H. Nakatsuji, X. Li, M. Caricato, A. Marenich, J. Bloino, B. Janesko, R. Gomperts, B. Mennucci, H. Hratchian, J. Ortiz, A. Izmaylov, J. Sonnenberg, D. Williams-Young, F. Ding, F. Lipparini, F. Egidi, J. Goings, B. Peng, A. Petrone, T. Henderson, D. Ranasinghe, V. Zakrzewski, J. Gao, N. Rega, G. Zheng, W. Liang, M. Hada, M. Ehara, K. Toyota, R. Fukuda, J. Hasegawa, M. Ishida, T. Nakajima, Y. Honda, O. Kitao, H. Nakai, T. Vreven, K. Throssell, J. Montgomery, J. Peralta, F. Ogliaro, M. Bearpark, J. Heyd, E. Brothers, K. Kudin, V. Staroverov, T. Keith, R. Kobayashi, J. Normand, K. Raghavachari, A. Rendell, J. Burant, S. Iyengar, J. Tomasi, M. Cossi, J. Millam, M. Klene, C. Adamo, R. Cammi, J. Ochterski, R. Martin, K. Morokuma, O. Farkas, J. Foresman, D. Fox, Gaussian 09, Revision D.01, Gaussian, Inc, Wallingford CT, 2016.
- [26] C. Lee, W. Yang, R. Parr, Development of the Colle-Salvetti correlation-energy formula into a functional of the electron density, *Phys. Rev. B* 37 (1988) 785–790, <https://doi.org/10.1103/PhysRevB.37.785>.
- [27] A. Becke, Density-functional exchange-energy approximation with correct asymptotic behavior, *Phys. Rev. A* 38 (1988) 3098–3100, <https://doi.org/10.1103/PhysRevA.38.3098>.
- [28] R. Ditchfield, W.J. Hehre, J.A. Pople, Self-consistent molecular-orbital methods. IX. An extended gaussian-type basis for molecular-orbital studies of organic molecules, *J. Chem. Phys.* 54 (1971) 720–723, <https://doi.org/10.1063/1.1674902>.
- [29] W.J. Hehre, K. Ditchfield, J.A. Pople, Self-consistent molecular orbital methods. XII. Further extensions of gaussian-type basis sets for use in molecular orbital studies of organic molecules, *J. Chem. Phys.* 56 (1972) 2257–2261, <https://doi.org/10.1063/1.1677527>.
- [30] M.M. Francl, W.J. Pietro, W.J. Hehre, J.S. Binkley, M.S. Gordon, D.J. DeFrees, J. A. Pople, Self-consistent molecular orbital methods. XXIII. A polarization-type basis set for second-row elements, *J. Chem. Phys.* 77 (1982) 3654–3665, <https://doi.org/10.1063/1.444267>.
- [31] M.S. Gordon, J.S. Binkley, J.A. Pople, I.W.J. Pietro, W.J. Hehre, Self-consistent molecular-orbital methods. 22. Small split-valence basis sets for second-row elements, *J. Am. Chem. Soc.* 104 (1982) 2797–2803.
- [32] P.C. Hariharan, J.A. Pople, The influence of polarization functions on molecular orbital hydrogenation energies, *Theor. Chim. Acta* 28 (1973) 213–222, <https://doi.org/10.1007/BF00533485>.
- [33] S.F. Sousa, P.A. Fernandes, M.J. Ramos, General performance of density functionals, *J. Phys. Chem. A* 111 (2007) 10439–10452, <https://doi.org/10.1021/jp0734474>.
- [34] S.F. Sousa, P.A. Fernandes, M.J. Ramos, Effective tailor-made force field parameterization of the several Zn coordination environments in the puzzling FTase enzyme: opening the door to the full understanding of its elusive catalytic mechanism, *Theor. Chem. Accounts* 117 (2007) 171–181, <https://doi.org/10.1007/s00214-006-0170-9>.
- [35] R.P.P. Neves, S.F. Sousa, P.A. Fernandes, M.J. Ramos, Parameters for molecular dynamics simulations of manganese-containing metalloproteins, *J. Chem. Theory Comput.* 9 (2013) 2718–2732, <https://doi.org/10.1021/ct400055v>.
- [36] D. Case, K. Belfon, I. Ben-Shalom, S. Brozell, D. Cerutti, T. Cheatham, V. Cruzeiro, T. Darden, R. Duke, D. Ghoreishi, G. Giambasu, T. Giese, M. Gilson, H. Gohlke, A. Goetz, D. Greene, R. Harris, N. Homeyer, Y. Huang, S. Izadi, A. Kovalenko, R. Krasny, T. Kurtzman, T. Lee, S. LeGrand, P. Li, C. Lin, J. Liu, T. Luchko, R. Luo, V. Man, D. Mermelstein, K. Merz, Y. Miao, G. Monard, H. Nguyen, A. Onufriev, F. Pan, R. Qi, D. Roe, A. Roitberg, C. Sagui, S. Schott-Verdugo, J. Shen, C. Simmerling, J. Smith, J. Swails, R. Walker, J. Wang, H. Wei, L. Wilson, R. Wolf, X. Wu, L. Xiao, Y. Xiong, D. York, P. Kollman, AMBER 19, University of California, San Francisco, 2019, <https://doi.org/10.1007/s10637-020-01020-2>.
- [37] J.A. Maier, C. Martinez, K. Kasavajhala, L. Wickstrom, K.E. Hauser, C. Simmerling, ff14SB: improving the accuracy of protein side chain and backbone parameters from ff99SB, *J. Chem. Theory Comput.* 11 (2015) 3696–3713, <https://doi.org/10.1021/acs.jctc.5b00255>.
- [38] J. Wang, R. Wolf, J. Caldwell, P. Kollman, D. Case, Development and testing of a general amber force field, *J. Comput. Chem.* 25 (2004) 1157–1174, <https://doi.org/10.1002/jcc.20035>.
- [39] D.S. Lemons, A. Gythiel, Paul Langevin’s 1908 paper “On the Theory of Brownian Motion” [“Sur la théorie du mouvement brownien,” *C. R. Acad. Sci. (Paris)* 146, 530–533 (1908)], *Am. J. Phys.* 65 (1997) 1079–1081, <https://doi.org/10.1119/1.18725>.
- [40] J.A. Izaguirre, D.P. Catarello, J.M. Wozniak, R.D. Skeel, Langevin stabilization of molecular dynamics, *J. Chem. Phys.* 114 (2001) 2090–2098, <https://doi.org/10.1063/1.1332996>.
- [41] M.J. Abraham, T. Murtola, R. Schulz, S. Páll, J.C. Smith, B. Hess, E. Lindah, Gromacs: High performance molecular simulations through multi-level parallelism from laptops to supercomputers, *SoftwareX*. 1–2 (2015) 19–25, <https://doi.org/10.1016/j.softx.2015.06.001>.
- [42] H.J.C. Berendsen, J.P.M. Postma, W.F. Van Gunsteren, A. Dinola, J.R. Haak, Molecular dynamics with coupling to an external bath, *J. Chem. Phys.* 81 (1984) 3684–3690, <https://doi.org/10.1063/1.448118>.
- [43] M. Parrinello, A. Rahman, Polymorphic transitions in single crystals: a new molecular dynamics method, *J. Appl. Phys.* 52 (1981) 7182–7190, <https://doi.org/10.1063/1.328693>.
- [44] B. Hess, H. Bekker, H.J.C. Berendsen, J.G.E.M. Fraaije, LINCS: a linear constraint Solver for molecular simulations, *J. Comput. Chem.* 18 (1997) 1463–1472, [https://doi.org/10.1002/\(SICI\)1096-987X\(199709\)18:12<1463::AID-JCC4>3.0.CO;2-H](https://doi.org/10.1002/(SICI)1096-987X(199709)18:12<1463::AID-JCC4>3.0.CO;2-H).
- [45] T. Vasanthakumar, S.A. Bueler, D. Wu, V. Beilstein-Edmands, C.V. Robinson, J. L. Rubinstein, Structural comparison of the vacuolar and Golgi V-ATPases from *Saccharomyces cerevisiae*, *Proc. Natl. Acad. Sci. U. S. A.* 116 (2019) 7272–7277, <https://doi.org/10.1073/pnas.1814818116>.
- [46] L. Wang, D. Wu, C.V. Robinson, H. Wu, T.-M. Fu, Structures of a complete human V-ATPase reveal mechanisms of its assembly, *Mol. Cell* 80 (2020) 501–511.e3, <https://doi.org/10.1016/j.molcel.2020.09.029>.
- [47] S. Schott-Verdugo, H. Gohlke, PACKMOL-Memgen: a simple-to-use, generalized workflow for membrane-protein-lipid-bilayer system building, *J. Chem. Inf. Model.* 59 (2019) 2522–2528, <https://doi.org/10.1021/acs.jcim.9b00269>.
- [48] S. Jo, J.B. Lim, J.B. Klauda, W. Im, CHARMM-GUI membrane builder for mixed bilayers and its application to yeast membranes, *Biophys. J.* 97 (2009) 50–58, <https://doi.org/10.1016/j.bpj.2009.04.013>.

- [49] C.J. Dickson, B.D. Madej, Å.A. Skjevik, R.M. Betz, K. Teigen, I.R. Gould, R. C. Walker, Lipid14: the amber lipid force field, *J. Chem. Theory Comput.* 10 (2014) 865–879, <https://doi.org/10.1021/ct4010307>.
- [50] D. Case, K. Belfon, I. Ben-Shalom, S. Brozell, D. Cerutti, T. Cheatham, V. Cruzeiro, T. Darden, R. Duke, G. Giambasu, M. Gilson, H. Gohlke, A. Goetz, R. Harris, S. Izadi, S. Izmailov, K. Kasavajhala, A. Kovalenko, R. Krasny, T. Kurtzman, T. Lee, S. LeGrand, P. Li, C. Lin, J. Liu, T. Luchko, R. Luo, V. Man, K. Merz, Y. Miao, O. Mikhailovskii, G. Monard, H. Nguyen, A. Onufriev, F. Pan, S. Pantano, R. Qi, D. Roe, A. Roitberg, C. Sagui, S. Schott-Verdugo, J. Shen, C. Simmerling, N. Skrynnikov, J. Smith, J. Swails, R. Walker, J. Wang, L. Wilson, R. Wolf, X. Wu, Y. Xiong, T. Xue, D. York, P. Kollman, *AMBER 2020*, 2020.
- [51] J.P. Ryckaert, G. Ciccotti, H.J.C. Berendsen, Numerical integration of the cartesian equations of motion of a system with constraints: molecular dynamics of n-alkanes, *J. Comput. Phys.* 23 (1977) 327–341, [https://doi.org/10.1016/0021-9991\(77\)90098-5](https://doi.org/10.1016/0021-9991(77)90098-5).
- [52] W. Humphrey, A. Dalke, K. Schulten, VMD: visual molecular dynamics, *J. Mol. Graph.* 14 (1996) 33–38, [https://doi.org/10.1016/0263-7855\(96\)00018-5](https://doi.org/10.1016/0263-7855(96)00018-5).
- [53] G.C.P. Van Zundert, J.P.G.L.M. Rodrigues, M. Trellet, C. Schmitz, P.L. Kastiritis, E. Karaca, A.S.J. Melquiond, M. Van Dijk, S.J. De Vries, A.M.J.J. Bonvin, The HADDOCK2.2 web server: user-friendly integrative modeling of biomolecular complexes, *J. Mol. Biol.* 428 (2016) 720–725, <https://doi.org/10.1016/j.jmb.2015.09.014>.
- [54] J. Roel-Touris, C.G. Don, R.R. Honorato, J.P.G.L.M. Rodrigues, A.M.J.J. Bonvin, Less is more: coarse-grained integrative modeling of large biomolecular assemblies with HADDOCK, *J. Chem. Theory Comput.* 15 (2019) 6358–6367, <https://doi.org/10.1021/acs.jctc.9b00310>.
- [55] J.P.G.L.M. Rodrigues, M. Trellet, C. Schmitz, P. Kastiritis, E. Karaca, A.S. J. Melquiond, A.M.J.J. Bonvin, Clustering biomolecular complexes by residue contacts similarity, *Proteins Struct. Funct. Bioinforma.* 80 (2012) 1810–1817, <https://doi.org/10.1002/prot.24078>.
- [56] A. Vangone, J.P.G.L.M. Rodrigues, L.C. Xue, G.C.P. van Zundert, C. Geng, Z. Kurkuoglu, M. Nellen, S. Narasimhan, E. Karaca, M. van Dijk, A.S.J. Melquiond, K.M. Visscher, M. Trellet, P.L. Kastiritis, A.M.J.J. Bonvin, Sense and simplicity in HADDOCK scoring: Lessons from CASP-CAPRI round 1, *Proteins Struct. Funct. Bioinf.* 85 (2017) 417–423, <https://doi.org/10.1002/prot.25198>.
- [57] W. Jorgensen, J. Tirado-Rives, The OPLS [optimized potentials for liquid simulations] potential functions for proteins, energy minimizations for crystals of cyclic peptides and crambin, *J. Am. Chem. Soc.* 110 (1988) 1657–1666, <https://doi.org/10.1021/ja00214a001>.
- [58] E. Wang, H. Sun, J. Wang, Z. Wang, H. Liu, J.Z.H. Zhang, T. Hou, End-point binding free energy calculation with MM/PBSA and MM/GBSA: strategies and applications in drug design, *Chem. Rev.* 119 (2019) 9478–9508, <https://doi.org/10.1021/acs.chemrev.9b00055>.
- [59] M. Sgobba, F. Caporuscio, A. Anighoro, C. Portioli, G. Rastelli, Application of a post-docking procedure based on MM-PBSA and MM-GBSA on single and multiple protein conformations, *Eur. J. Med. Chem.* 58 (2012) 431–440, <https://doi.org/10.1016/j.ejmech.2012.10.024>.
- [60] B.R. Miller, T.D. McGee, J.M. Swails, N. Homeyer, H. Gohlke, A.E. Roitberg, MMPBSA.py: An efficient program for end-state free energy calculations, *J. Chem. Theory Comput.* 8 (2012) 3314–3321, <https://doi.org/10.1021/ct300418h>.
- [61] J. Weiser, P.S. Shenkin, W.C. Still, Approximate atomic surfaces from linear combinations of pairwise overlaps (LCPO), *J. Comput. Chem.* 20 (1999) 217–230, [https://doi.org/10.1002/\(SICI\)1096-987X\(19990130\)20:2<217::AID-JCC4>3.0.CO;2-A](https://doi.org/10.1002/(SICI)1096-987X(19990130)20:2<217::AID-JCC4>3.0.CO;2-A).
- [62] S.C. Shoemaker, N. Ando, X-rays in the cryo-electron microscopy era: structural biology's dynamic future, *Biochemistry* 57 (2018) 277–285, <https://doi.org/10.1021/acs.biochem.7b01031>.
- [63] M. Torchala, T. Gerguri, R.A.G. Chaleil, P. Gordon, F. Russell, M. Keshani, P. A. Bates, Enhanced sampling of protein conformational states for dynamic cross-docking within the protein-protein docking server SwarmDock, *Proteins Struct. Funct. Bioinf.* 88 (2020) 962–972, <https://doi.org/10.1002/prot.25851>.
- [64] C. Nhan, C.J. Rix, B.K. May, A. Hung, Temperature-induced structural changes of apo-lactoferrin and their functional implications: a molecular dynamics simulation study, *Mol. Simul.* 45 (2019) 533–548, <https://doi.org/10.1080/08927022.2018.1562187>.
- [65] C. Nhan, D.M. Small, B.K. May, A. Hung, pH-induced structural changes of apo-lactoferrin and implications for its function: a molecular dynamics simulation study, *Mol. Simul.* 45 (2019) 87–103, <https://doi.org/10.1080/08927022.2018.1535178>.
- [66] P. Pomastowski, M. Sprynsky, P. Žuvela, K. Rafinska, M. Milanowski, J.J. Liu, M. Yi, B. Buszewski, Silver-lactoferrin nanocomplexes as a potent antimicrobial agent, *J. Am. Chem. Soc.* 138 (2016) 7899–7909, <https://doi.org/10.1021/jacs.6b02699>.
- [67] S. Kubo, T. Niina, S. Takada, Molecular dynamics simulation of proton-transfer coupled rotations in ATP synthase FO motor, *Sci. Rep.* 10 (2020) 1–16, <https://doi.org/10.1038/s41598-020-65004-1>.
- [68] Y. Isaka, T. Ekimoto, Y. Kokabu, I. Yamato, T. Murata, M. Ikeguchi, Rotation mechanism of molecular motor V1-ATPase studied by multiscale molecular dynamics simulation, *Biophys. J.* 112 (2017) 911–920, <https://doi.org/10.1016/j.bpj.2017.01.029>.
- [69] K. Condic-Jurkic, N. Subramanian, A.E. Mark, M.L. O'Mara, The reliability of molecular dynamics simulations of the multidrug transporter P-glycoprotein in a membrane environment, *PLoS One.* 13 (2018) 1–24, <https://doi.org/10.1371/journal.pone.0191882>.
- [70] S. Arai, S. Saijo, K. Suzuki, K. Mizutani, Y. Kakinuma, Y. Ishizuka-Katsura, N. Ohsawa, T. Terada, M. Shirouzu, S. Yokoyama, S. Iwata, I. Yamato, T. Murata, Rotation mechanism of *Enterococcus hirae* V1-ATPase based on asymmetric crystal structures, *Nature* 493 (2013) 703–707, <https://doi.org/10.1038/nature11778>.
- [71] T. Vasanthakumar, J.L. Rubinstein, Structure and roles of V-type ATPases, *Trends Biochem. Sci.* 45 (2020) 295–307, <https://doi.org/10.1016/j.tibs.2019.12.007>.
- [72] T. Pansar, A. Poso, Binding affinity via docking: fact and fiction, *Molecules* 23 (2018) 1899, <https://doi.org/10.3390/molecules23081899>.
- [73] M.J.R. Yunta, Docking and ligand binding affinity: uses and pitfalls, *Am. J. Model. Optim.* 4 (2016) 74–114, <https://doi.org/10.12691/ajmo-4-3-2>.
- [74] M. Shen, S. Zhou, Y. Li, P. Pan, L. Zhang, T. Hou, Discovery and optimization of triazine derivatives as ROCK1 inhibitors: molecular docking, molecular dynamics simulations and free energy calculations, *Mol. Biosyst.* 9 (2013) 361–374, <https://doi.org/10.1039/c2mb25408e>.
- [75] X. Zhang, H. Perez-Sanchez, F. Lighstone, A comprehensive docking and MM/GBSA rescoring study of ligand recognition upon binding antithrombin, *Curr. Top. Med. Chem.* 17 (2017) 1631–1639, <https://doi.org/10.2174/1568026616666161171>.
- [76] A. Suenaga, N. Okimoto, Y. Hirano, K. Fukui, An efficient computational method for calculating ligand binding affinities, *PLoS One.* 7 (2012), <https://doi.org/10.1371/journal.pone.0042846>.
- [77] M. Aamir, V.K. Singh, M.K. Dube, M. Meena, S.P. Kashyap, S.K. Katari, R. S. Upadhyay, A. Umamaheswari, S. Singh, In silico prediction, characterization, molecular docking, and dynamic studies on fungal SDRs as novel targets for searching potential fungicides against fusarium wilt in tomato, *Front. Pharmacol.* 9 (2018) 1–28, <https://doi.org/10.3389/fphar.2018.01038>.
- [78] S.K. Mishra, J. Koca, Assessing the performance of MM/PBSA, MM/GBSA, and QM-MM/GBSA approaches on protein/carbohydrate complexes: effect of implicit solvent models, QM methods, and entropic contributions, *J. Phys. Chem. B* 122 (2018) 8113–8121, <https://doi.org/10.1021/acs.jpcc.8b03655>.
- [79] G. Weng, E. Wang, F. Chen, H. Sun, Z. Wang, T. Hou, Assessing the performance of MM/PBSA and MM/GBSA methods. 9. Prediction reliability of binding affinities and binding poses for protein-peptide complexes, *Phys. Chem. Chem. Phys.* 21 (2019) 10135–10145, <https://doi.org/10.1039/c9cp01674k>.
- [80] A.A. Elmaaty, R. Alnajjar, M.I.A. Hamed, M. Khattab, M.M. Khalifa, A.A. Al-Karmalawy, Revisiting activity of some glucocorticoids as a potential inhibitor of SARS-CoV-2 main protease: theoretical study, *RSC Adv.* 11 (2021) 10027–10042, <https://doi.org/10.1039/d0ra10674g>.
- [81] Z. Gao, Y. Du, X. Sheng, J. Shen, Molecular dynamics simulations based on 1-phenyl-4-benzoyl-1-hydro-triazole inverse agonists, *Int. J. Mol. Sci.* 22 (2021), <https://doi.org/10.3390/ijms22073724>.
- [82] H.M. Wu, F.C. Church, Arginine 25 and Arginine 28 of lactoferrin are critical for effective heparin neutralization in blood, *Arch. Biochem. Biophys.* 412 (2003) 121–125, [https://doi.org/10.1016/S0003-9861\(03\)00035-3](https://doi.org/10.1016/S0003-9861(03)00035-3).
- [83] D.M. Mann, E. Romm, M. Migliorini, Delineation of the glycosaminoglycan-binding site in the human inflammatory response protein lactoferrin, *J. Biol. Chem.* 269 (1994) 23661–23667, [https://doi.org/10.1016/s0021-9258\(17\)31566-1](https://doi.org/10.1016/s0021-9258(17)31566-1).
- [84] O. Senkovich, W.J. Cook, S. Mirza, S.K. Hollingshead, I.I. Protasevich, D.E. Briles, D. Chattopadhyay, Structure of a complex of human lactoferrin N-lobe with pneumococcal surface protein a provides insight into microbial defense mechanism, *J. Mol. Biol.* 370 (2007) 701–713, <https://doi.org/10.1016/j.jmb.2007.04.075>.
- [85] E. Ellass-Rochard, A. Roseanu, D. Legrand, M. Trif, V. Salmon, C. Motas, J. Montreuil, G. Spik, Lactoferrin-lipopolysaccharide interaction: Involvement of the 28–34 loop region of human lactoferrin in the high-affinity binding to *Escherichia coli* 055B5 lipopolysaccharide, *Biochem. J.* 312 (1995) 839–845, <https://doi.org/10.1042/bj3120839>.
- [86] N.K.H. Ostan, R.H. Yu, D. Ng, C.C.L. Lai, A.K. Pogoutse, V. Sarpe, M. Hepburn, J. Sheff, S. Raval, D.C. Schriener, T.F. Moraes, A.B. Schryvers, Lactoferrin binding protein B – a bi-functional bacterial receptor protein, *PLoS Pathog.* 13 (2017), <https://doi.org/10.1371/journal.ppat.1006244>.
- [87] H. Wong, A.B. Schryvers, Bacterial lactoferrin-binding protein a binds to both domains of the human lactoferrin C-lobe, *Microbiology* 149 (2003) 1729–1737, <https://doi.org/10.1099/mic.0.26281-0>.
- [88] R. Mir, N. Singh, G. Vikram, M. Sinha, A. Bhushan, P. Kaur, A. Srinivasan, S. Sharma, T.P. Singh, Structural and binding studies of C-terminal half (C-lobe) of lactoferrin protein with COX-2-specific non-steroidal anti-inflammatory drugs (NSAIDs), *Arch. Biochem. Biophys.* 500 (2010) 196–202, <https://doi.org/10.1016/j.jabb.2010.05.026>.
- [89] R. Mir, R.P. Kumar, N. Singh, G.P. Vikram, M. Sinha, A. Bhushan, P. Kaur, A. Srinivasan, S. Sharma, T.P. Singh, Specific interactions of C-terminal half (C-lobe) of lactoferrin protein with edible sugars: binding and structural studies with implications on diabetes, *Int. J. Biol. Macromol.* 47 (2010) 50–59, <https://doi.org/10.1016/j.jbiomac.2010.03.021>.
- [90] K. Suzuki, K. Mizutani, S. Maruyama, K. Shimono, F.L. Imai, E. Muneyuki, Y. Kakinuma, Y. Ishizuka-Katsura, M. Shirouzu, S. Yokoyama, I. Yamato, T. Murata, Crystal structures of the ATP-binding and ADP-release dwells of the V1 rotary motor, *Nat. Commun.* 7 (2016) 13235, <https://doi.org/10.1038/ncomms13235>.
- [91] J. Zhao, K. Beyrakhova, Y. Liu, C.P. Alvarez, S.A. Bueler, L. Xu, C. Xu, M. T. Boniecki, V. Kanelis, Z.Q. Luo, M. Cygler, J.L. Rubinstein, Molecular basis for the binding and modulation of V-ATPase by a bacterial effector protein, *PLoS Pathog.* 13 (2017) 1–21, <https://doi.org/10.1371/journal.ppat.1006394>.
- [92] L. Ding, Z. Guo, H. Xu, T. Li, Y. Wang, H. Tao, The inhibitory effect of celastrolin V on the ATP hydrolytic activity of the complex of V-ATPase subunits a and b in the

- midgut of *Mythimna separata*, *Toxins* (Basel). 11 (2019), <https://doi.org/10.3390/toxins11020130>.
- [93] M.T. Andrés, J.F. Fierro, Antimicrobial mechanism of action of transferrins: selective inhibition of H⁺-ATPase, *Antimicrob. Agents Chemother.* 54 (2010) 4335–4342, <https://doi.org/10.1128/AAC.01620-09>.
- [94] M. Nakanishi-Matsui, M. Sekiya, R.K. Nakamoto, M. Futai, The mechanism of rotating proton pumping ATPases, *Biochim. Biophys. Acta Bioenerg.* 1797 (2010) 1343–1352, <https://doi.org/10.1016/j.bbabi.2010.02.014>.